Geometry of sedimentary deposits and evolution of the landforms in the Chobe Enclave, Northern Botswana

Thuto Mokatse [a,*], Shlomy Vainer [a], James Irving [b], Christoph Schmidt [a], Boniface Kgosidintsi [c], Elisha Shemang [c], Eric P. Verrecchia [a]

[a] Institute of Earth Surface Dynamics — IDYST, FGSE, University of Lausanne, 1015 Lausanne, Switzerland
[b] Institute of Earth Sciences — ISTE, FGSE, University of Lausanne, 1015 Lausanne, Switzerland
[c] Earth and Environmental Sciences, Botswana International University of Science and Technology, Botswana

ARTICLE INFO

ABSTRACT

The imprint of neotectonics is frequently obscured in low-relief environments by the sedimentary cover. This is the case in the Chobe Enclave, part of a pristine region of the Middle Kalahari Basin in northern Botswana, where numerous fossil landforms, such as sand dunes, pans, sand ridges, and carbonate islands, can be observed but whose detailed origins are unclear. In this study, a combination of near-surface geophysical surveys, sedimentological analysis, and optically-stimulated luminescence (OSL) dating were used to study the relationship between landscape development and neotectonic activity in one region of the Chobe Enclave. Specifically, electrical resistivity tomography (ERT) and ground penetrating radar (GPR) surveys were used to define the lateral and vertical distribution of sedimentary deposits associated with a prominent sand ridge and its margins. Sedimentological analysis and OSL dating of soil samples from pits taken along the survey lines were then used to calibrate the geophysical results and establish a chronostratigraphical framework. Our results lead to the following hypotheses regarding the evolution of the Chobe landscape: (i) during the Late Pleistocene (>~25 ka), fluvial channels were buried due to epeirogenic movements, resulting in paleo-channels; (ii) between ~25 ka and ~6 ka, a paleo-lake shoreline formed, which resulted in the linear eastern margin observed on the considered sand ridge. Erosional bounding surfaces suggest the syndepositional uplift of the sand ridge morphologies during this time; (iii) a neotectonic influence on the evolution of the landscape is revealed by the incision of the sand ridge forming fluvial watergaps since ~6 ka ago; and (iv) due to continuous aeolian and fluvial reworking, the western-most ridge became gradually isolated from the floodplain resulting in an inherited relief. In conclusion, this investigation allowed the deformation caused by epeirogenic movements acting on a low relief landscape to be characterized in terms of landforms and sedimentary body properties.

1. Introduction

Recent and ongoing tectonics can affect landscape-shaping processes and their resultant landforms at various scales (Keller and Pinter, 1996; Holbrook and Schumm, 1999; Schumm et al., 2002). However, the imprint of neotectonics is frequently obscured in low-relief environments by the sedimentary cover, hampering identification of the origin of different landforms (Ruszkiczay-Rüdiger et al., 2009). Tectonically influenced landscapes are usually identified by a series of geomorphological indicators, such as entrenched channels, a high degree of incision along the channels flowing across active faults, or a sudden change in channel morphology (e.g., Rhea, 1993; Schumm et al., 2002; Bishop

et al., 2003; Riquelme et al., 2003; Silva et al., 2003). The Chobe Enclave, situated in northern Botswana, is bounded by the Chobe and Linyanti faults and has a generally flat topography (Fig. 1a-d). It has a variety of landforms, most notable of which are sand ridges, which have been previously interpreted as relict beach ridges of a former lacustrine environment (Shaw and Thomas, 1988; Burrough and Thomas, 2008). The significance of these sand ridges for palaeoenvironmental and palaeoclimatological reconstructions was outlined in the context of OSL-derived lake stage chronologies (Burrough and Thomas, 2008). A tectonic origin for the topographic variations along the ridges in the region was also mentioned (Gumbricht et al., 2001). While all of this work has brought improved understanding of the origin of the sand ridges in the

---

Chobe Enclave, the details regarding the influence of tectonics on their development, and on the landscape evolution in general, have been largely ignored. Further, the way that the internal architecture of these sand ridges could have been affected by neotectonics (McFarlane and Eckardt, 2007; Nash and Eckardt, 2015; Eckardt et al., 2016) remains unclear. Therefore, there is a noticeable knowledge gap concerning the occurrence and impact of neotectonic activity in the Chobe Enclave. This is addressed in this work, which represents a case study for understanding the propagation of upper crust deformation in incipient rifting settings and the resultant effect on landforms.
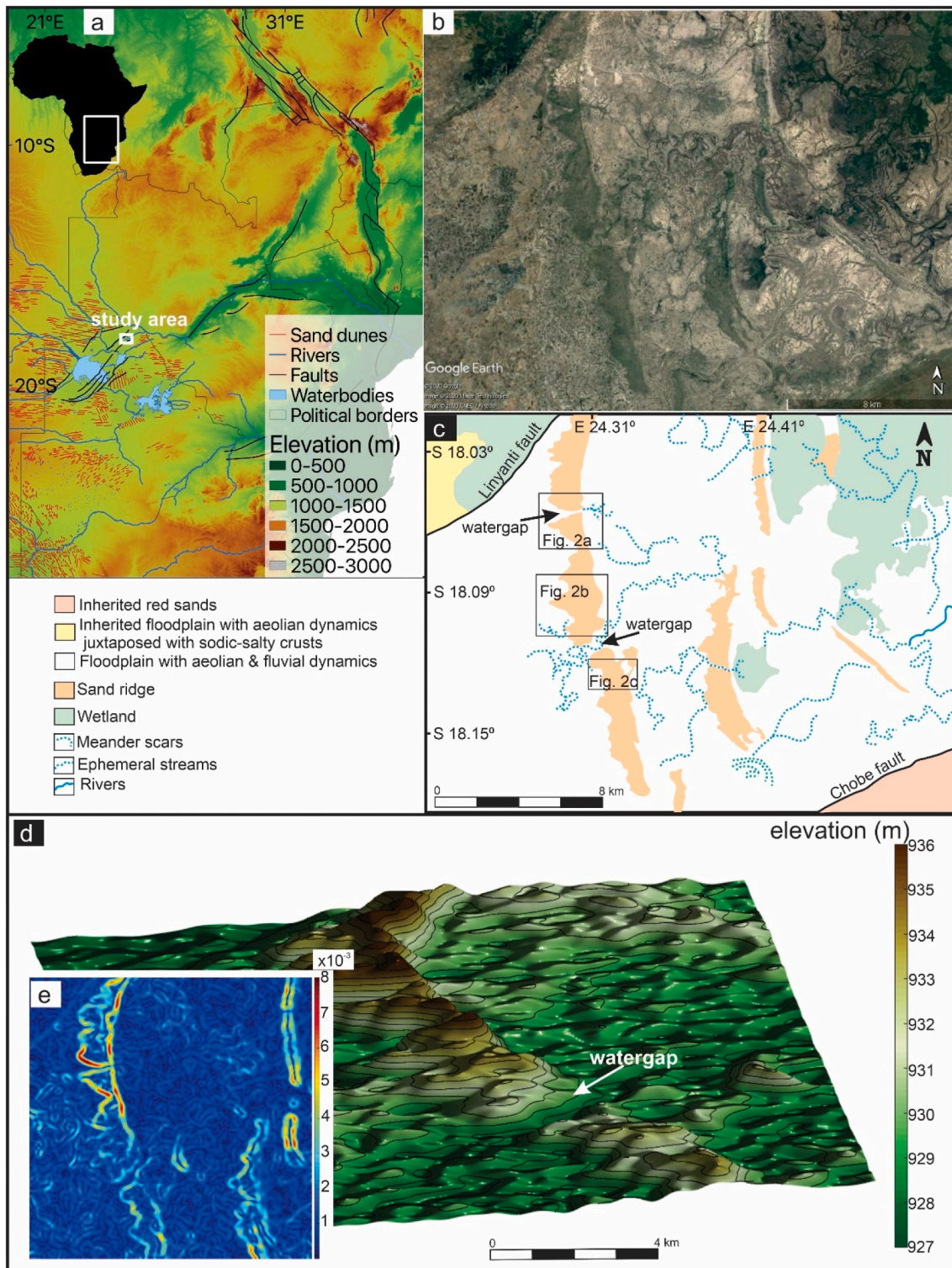

Fig. 1. (a) Main rivers, sand dune fields, and faults superimposed on the topography of southern Africa based on SRTM 30 s DEM (NASA JPL, 2013). Faults of the East African Rift System (EARS) are after Chorowicz (2005) and their possible extension to the Okavango Graben (OG) are modified from Kinabo et al. (2008). (b) Satellite image of the study area (Google Earth, 2020). (c) Geomorphological interpretation of the area depicting main landforms with localities of study sites mentioned in Fig. 2. (d) Digital elevation model of the studied sand ridge and adjacent floodplain constructed from Google Earth data. (e) Slope values of the western part of Fig. 1b and c.

In this study, we focus on the western-most sand ridge, which is the main geomorphological feature in the Chobe Enclave (Fig. 1c). We use a combination of near-surface geophysical surveys, optically-stimulated luminescence (OSL) dating, and sedimentological analyses to study the structure, lithostratigraphy, and chronology of this ridge. The main objectives of our work are: (i) to define the lateral and vertical distribution of sedimentary bodies and the boundaries of the various lithologies; (ii) to outline the possible presence of structures that could be related to neotectonic processes; and (iii) to document the influence of different deformational mechanisms. To this end, we conducted electrical resistivity tomography (ERT) and ground-penetrating radar (GPR) surveys over various parts of the ridge, where sediment samples were collected for OSL dating and sedimentological analyses. Together, these four methods provide highly complementary information for the characterization of Quaternary sediments (e.g., Aitken, 1998; Baines et al., 2002; Wisen et al., 2005; Bristow et al., 2005, 2007; Burrough and Thomas, 2008; Bristow, 2009). The establishment of a chronostratigraphical framework allows the temporal development of the inspected landforms to be drawn, ultimately gaining understanding about their evolution within the context of regional processes.

2. Geological setting

2.1. Structural context of the Chobe Enclave

On a regional scale, the Chobe Enclave is situated in the Middle Kalahari Basin, where several deformational mechanisms of different amplitude and temporal reoccurrence exist. Occupying the largest portion of the Intracratonic Kalahari Basin (Vainer et al., 2018), the Middle Kalahari is breached by the southwestward propagation of the more discretely deformed East African Rift System (EARS), and is considered to represent settings typical of incipient rifting (Fairhead and Girdler, 1969; Huntsman-Mapila et al., 2009; Kinabo et al., 2008; Fig. 1a). Based on the structures of the underlying mantle and crust, the Middle Kalahari is classified as a passive rift (Yu et al., 2015a, 2015b, 2017). The basin that overlies Proterozoic and Mesozoic rift structures (Dixey, 1956; Modisi et al., 2000; Doucouré and de Wit, 2003) is situated between elevated structural arches (Gumbricht et al., 2001). This led recent seismic tomography and magnetotelluric studies to suggest that deformation is triggered by inter-cratonic strains between the surrounding Archean cratons (Pastier et al., 2017; Yu et al., 2017). The differential deformation of the uplifted structural axes within the Kalahari Basin (Moore, 1999) resulted in the formation of several sub-basins, including the Makgadikgadi-Okavango-Zambezi basin (MOZB; McCarthy, 2013; Ringrose et al., 2005) of the Middle Kalahari, that was established in the early Pleistocene (Vainer et al., 2021a). The later segmentation of the MOZB into the current configuration that occupies the Chobe Enclave (Fig. 1b, c) is the result of Quaternary tectonics, which is assumed to be reflected in the sedimentary bodies that occupy this structural trough. Like the more developed basins in the EARS, grabens and half grabens provide space for sedimentation and the accumulation of waterbodies, whereas transfer zones link the depressed blocks and transport displacement strains between individual fault and basin segments (Gawthorpe and Hurst, 1993; McCarthy, 2013). Locally, the Chobe Enclave is bounded by the Linyanti (to the northwest) and the Chobe (to the southeast) faults (Fig. 1c), which breach the vast intracratonic Kalahari Basin to form this sub-basin within the high African plateau (Fig. 1a). Together with the Ngami and Mababe sub-basins, the Chobe Enclave comprises a syntectonic depocenter within the structural depression of the Okavango Graben (OG), which is the northern segment of the larger MOZB. This structural depression is made up of a series of NE-SW trending normal to dextral strike-slip faults (Modisi et al., 2000; Campbell et al., 2006; Bufford et al., 2012). The bounding faults of the OG on the southern part that extends into the Chobe Enclave were formed in an *en-echelon* pattern with a direction following the strike of the Precambrian basement structures (Mallick et al., 1981; Moorkamp

et al., 2019). The OG has been associated with the formation of the southwestern branch of the EARS (Modisi et al., 2000; Alvarez Naranjo and Hogan, 2013). However, Pastier et al. (2017) argued that the tectonic structure of the OG better fits a transtensional basin model. Kinabo et al. (2008) coupled analysis of Shuttle Radar Topography Mission, Digital Elevation Model, and aeromagnetic data in the Chobe Enclave and revealed the development of soft linkage on segments of the Linyanti fault and evidence of a hard linkage forming between two *en-echelon* right-stepping segments of the Chobe fault.

2.2. Surficial geology and geomorphology of the Chobe Enclave

The Chobe Enclave was developed within the vast (10^6 km^2), elevated (~1000 m asl), erosional surface of the Central African Plateau, which was established by the Pliocene (Partridge, 1998; Burke and Gunnell, 2008; Daly et al., 2020) following discrete epeirogenic flexuring (Vainer et al., 2018, 2021a). Although later tectonic activity occurred, the general topography of the Chobe Enclave remains fairly flat. Even so, fluvial watergaps serve as notable geomorphological indicators in the Chobe Enclave and attribute for tectonic influence on the landscape, evidenced by incision across sand ridges (Fig. 1d). Two slopes are predominant in the area, one gently decreases from SW to NE, and the other from NW to SE, with a value of <0.02 % on average (Fig. 1e). This configuration promotes the existence of anastomosed fluvial systems, which are completely dry in the western part and become ephemeral to permanently flowing rivers to the east (Fig. 1b, c). The Chobe Enclave is mostly covered by unconsolidated sand that was introduced to the southern parts of the Kalahari approximately 2 Ma ago (Vainer et al., 2021b).

Cenozoic deposition of Kalahari Group sediments in the Chobe Enclave resulted in the accumulation of alluvial, lacustrine, fluvial, and aeolian deposits (Huntsman-Mapila et al., 2005; Podgorski et al., 2013). Sand ridges are the dominant landforms in the area (Mokatse et al., 2022), and are considered to represent late Quaternary paleolacustrine shorelines (Shaw and Thomas, 1988) formed under hydrological conditions different from the present-day (Grove, 1969; Cooke, 1980; Mallick et al., 1981; Shaw and Cooke, 1986; Shaw et al., 1988, 1997; Ringrose et al., 1999, 2005, 2009; Burrough and Thomas, 2008; Burrough et al., 2009; Moore et al., 2012). These ridges have been mostly studied in order to understand how they might relate to paleohydrological and paleoclimatological processes (Fig. 1c; Burrough et al., 2007; Burrough and Thomas, 2008).

The Chobe Enclave also includes carbonate deposits in an otherwise large siliceous-dominated basin. These deposits, which were described as palustrine limestones (Diaz et al., 2019), outcrop in the landscape as "*islands*" among the sands and are mostly observed in the central part of the Chobe Enclave, between the paleo-floodplain in the west and the large present-day floodplain in the east (Mokatse et al., 2022). These "islands" are also associated with diatomites in an unclear geometrical relationship, suggesting periods of wetter conditions and increased flows into the basin from the Chobe and Zambezi fluvial systems. Such paleo-flows likely contributed to the formation of lacustrine/palustrine deposits and were presumably developing during the surge of paleolakes witnessed in the south and the east of the Chobe Enclave by Burrough et al. (2009).

3. Methods

3.1. Site selection

This study focuses on the western-most north-south-trending sand ridge in the Chobe Enclave (Fig. 1c–e). Two key locations were targeted for data acquisition: (i) the sand ridge itself, to record morphological characteristics, which are critical to explain its origin and changes with time, and (ii) the sand ridge margins, which are pertinent to observe changes across the contact between the ridge and the floodplain.

3.2. Geophysical surveys

3.2.1. Electrical resistivity tomography (ERT)

ERT is an efficient and non-invasive geophysical technique that has been widely employed to image the spatial distribution of electrical resistivity in the shallow subsurface (e.g., Barber and Brown, 1984; Loke and Barker, 1996; Storz et al., 2000). In August 2020, a total of 6 ERT surveys were conducted in the study region (Fig. 2). Four of these surveys (ERT3, 4, 5 and 6) were at the sand ridge margins, where a transition from the fine sand of the ridge to the silt-rich sediments of the floodplain was recorded, whereas two surveys (ERT1 and 2) were acquired on the sand ridge itself. The latter two surveys represented regions where ERT imaging was possible on the sand ridge. In other locations, the highly resistive nature of the sand did not permit current flow into the ground, despite attempts to improve electrode coupling by watering with saline solution.

The ERT measurements were carried out using an IRIS Syscal Pro Switch 48-channel resistivity meter. The electrode spacing along the profiles was set to either 1 m or 2 m, and data were acquired using both the dipole-dipole and Wenner–Schlumberger electrode array configurations (Table 1). A Leica Geosystems differential GPS was used to measure the precise location and elevation of each electrode. Profiles ERT-1 and ERT-2, for which the line length exceeds the spacing times the number of available electrodes, were collected using a roll-along strategy. A pulse duration of 500 ms and a target of 50 mV for the potential readings were set as criteria for the current injection. For each resistivity quadripole, a total of four repeat measurements were performed in order to improve data quality and to help identify erroneous values.

Pre-processing of the ERT data was carried out using the Prosys II software and included deleting all resistance values where the relative standard deviation of the repeat quadripole measurements was >3 %, or where the measured electric potential had a value <5 mV. In order to prepare the data for the 2D inversion procedure, the precise x-y locations of each electrode were also projected onto a best-fitting straight line. To invert the measurements, the Boundless Electrical Resistivity Tomography (BERT) software package was employed (Günther and Rücker, 2019). The prior constraints placed on the resistivity model for the inversion were carefully evaluated and the same inversion settings were used for all of the apparent resistivity datasets. Specifically, we considered smooth (L2-norm) prior model constraints with the inversion parameter *zweight* set to 0.5 in order to reflect a balance between an isotropic (*zweight* = 1) and strongly layered (*zweight* = 0.1) resistivity distribution. Moreover, the regularization parameter *lambda,* which controls the balance between fitting the ERT measurements and respecting the prior smoothness constraints, was chosen to provide a normalized chi-squared data misfit approximately equal to one, in accordance with the assumed level of error on the potential measurements. Interpretation of the models was aided by lithological logs from pits acquired along the survey lines (Fig. 2).

3.2.2. Ground penetrating radar (GPR)

GPR allows the imaging of changes in electrical properties near the Earth's surface by recording the reflections of an emitted electromagnetic pulse from subsurface interfaces across which such properties change (Annan and Davis, 1992; Neal, 2004). Two GPR profiles were acquired at the study site (Fig. 2). Both were located on the sand ridge, where fine sand contributes to a highly electrically resistive environment which is ideally suited for GPR surveying. In contrast, at the sand ridge margins, the GPR method was not applicable because of the presence of silt-rich floodplain sediments, whose high electrical conductivity strongly attenuated the propagating GPR pulse.

The GPR data acquisition was carried out using a Mala ProEx system with 100 MHz rugged terrain antennas, which was connected to a GPS. The 100 MHz antennas allowed for a depth of penetration of approximately 12 m and were chosen because of their higher resolution compared to lower frequency antennas available for the same system

(Neal, 2004). The spacing between the transmitter and receiver antennas was 2.2 m. Data were recorded using a 500 ns time window and each recorded trace was stacked 16 times in order to improve the signal-to-noise ratio (Table 2). Traces were acquired continuously while moving the antennas at an approximately constant speed, resulting in an average trace spacing along the profile of roughly 14 cm.

The GPR datasets were processed using the ReflexW software. The processing was rather standard and consisted of the following steps: (i) data binning to create an even trace spacing; (ii) "dewow" to remove the low-frequency transient upon which the GPR reflections are superimposed; (iii) time-zero adjustment to calibrate the data to the emission time of the transmitted pulse; (iv) application of a time-varying gain function to compensate for attenuation and the geometrical spreading of energy; (v) frequency-wavenumber migration (Stolt, 1978) using a constant velocity of 0.15 m/ns in order to collapse diffraction hyperbolae and to reposition reflectors to their correct positions in depth; and (vi) correction for topography along the profile.

3.3. Sample analyses

3.3.1. Pit sample analyses

Six pit sites were located along the ERT and GPR survey lines to provide a ground control of the lithology (Fig. 2). This is a pertinent way to contribute to a well-informed interpretation of the various lithologies and to the assessment of the spatial distribution of surficial sediments. The characterization of the pit sites was based on field observations and particle size distribution (PSD) analyses carried out on 35 samples. The PSD were obtained using a laser diffraction Beckmann Coulter LS 13320 on the <2 mm size fraction after leaching with 10 % hydrochloric acid. Samples were first classified under the Folk's (1954) classification scheme as general descriptors, and statistics calculated using the Folk and Ward formula (Folk and Ward, 1957). The processing of PSD data was conducted to confirm the differences between the various position of groups of samples from the sand ridge and its margins. This was done by using various modes of their PSD, which essentially aided to identify the origin of the sediments. The PSD curves were all plotted together in order to observe the overall variations of their shapes. Moreover, End-Member Mixing Analysis (EMMA) was performed based on the algorithm provided by Dietze et al. (2012) and run within the MATLAB computing environment. It was applied to all PSD curves to recognize the possible contributions of the various sedimentary sources. After identification of the end-members, each sample was described in terms of relative contribution of each end-member to its PSD. Sediments associated with a specific sedimentary process usually have a characteristic PSD referred as an end member. Essentially, the observed PSD can be considered as a result of a mixing process of a finite number of end members resulting in a complex spectrum. EMMA of sediment PSD demonstrates one way of discretizing the continuum of selective entrainment, transport, and deposition of sediments, providing deeper insights into the sedimentary environment and climatic conditions involved (Prins et al., 2002, 2007; Dietze et al., 2013a, 2013b; Schmidt et al., 2021).

3.3.2. Optically stimulated luminescence (OSL)

3.3.2.1. Sampling and preparation.
One to two samples were collected from each pit to determine through OSL dating when the detrital material was last exposed to sunlight (Aitken, 1998). Sampling was completed using light-sealed tubes hammered into pit walls, at least 30 cm above the carbonate deposits, where present. Samples were then dry-sieved in subdued red-light conditions into the 180–212 μm size fraction. Quartz was isolated by dissolving carbonate and oxidizing organic matter with 10 % HCl and 30 % H_2O_2, respectively, and from other minerals by two-step heavy liquid separation using sodium polytungstate. The fraction with a density between 2.62 and 2.70 g cm^{-3} was
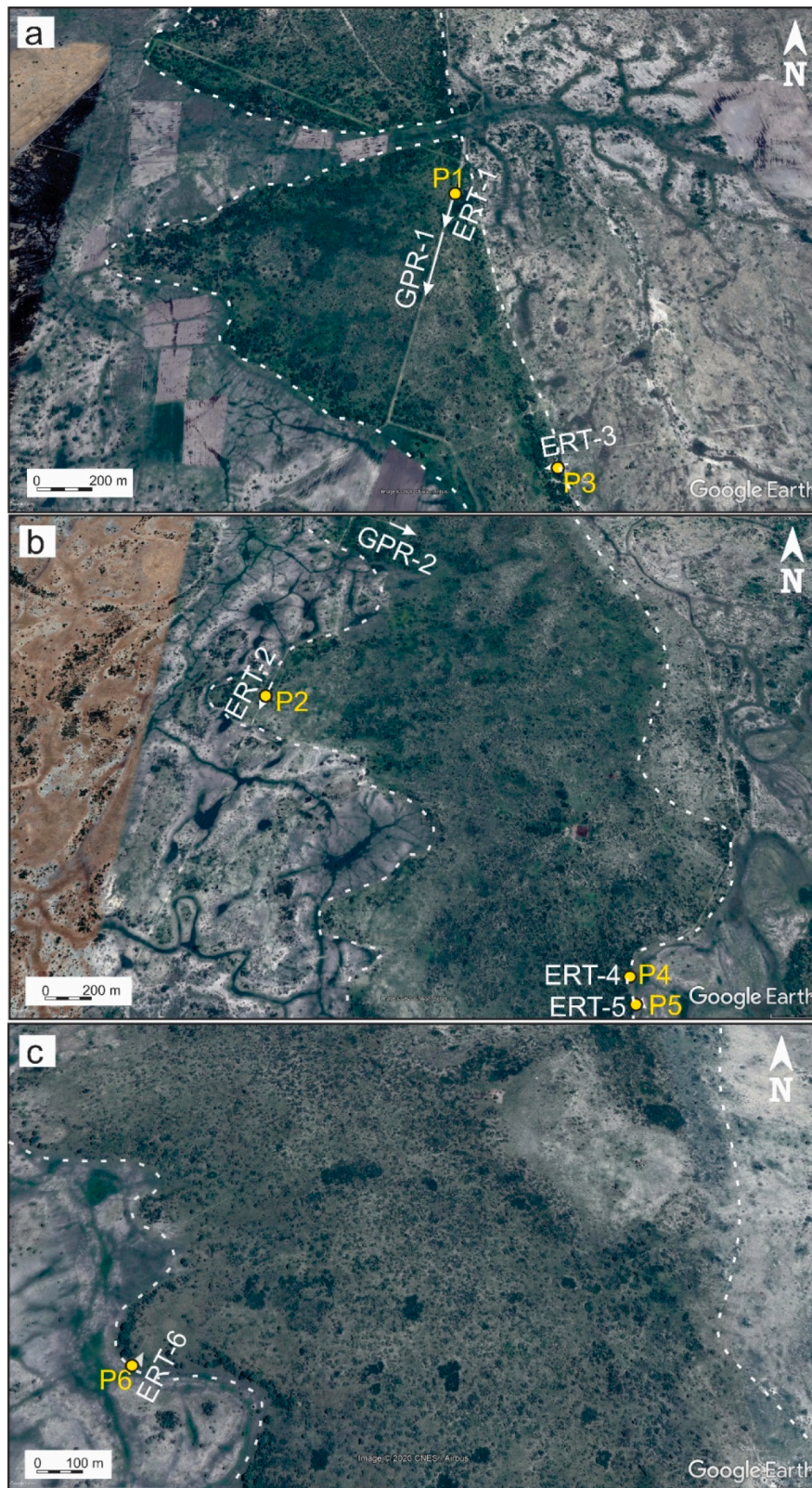
Fig. 2. Satellite images (Google Earth, 2020) showing the locations of ERT and GPR survey lines and corresponding pits (P). White arrows represent the direction and distance of geophysical surveys on the ground. White dashed lines represent the margins of the western-most sand ridge in the Chobe Enclave. The locations of images (a), (b) and (c) are shown in Fig. 1(c).

Table 1

Characteristics of the ERT profile lines considered in this study.

Profile line	Profile orientation	Profile length (m)	Number of electrodes	Electrode spacing (m)	Electrode array
ERT-1	NE–SW	214	48	2	Dipole-dipole & Wenner-Schlumberger
ERT-2	NE–SW	214	48	2	Dipole-dipole & Wenner-Schlumberger
ERT-3	E–W	94	48	2	Dipole-dipole & Wenner-Schlumberger
ERT-4	E–W	47	48	1	Dipole-dipole & Wenner-Schlumberger
ERT-5	E–W	47	48	1	Dipole-dipole & Wenner-Schlumberger
ERT-6	SW–NE	47	48	1	Dipole-dipole & Wenner-Schlumberger

etched for 40 min with 40 % HF and subsequently treated with 10 % HCl for dissolution of potential Ca-fluoride precipitates.

3.3.2.2. Equivalent dose estimation. Luminescence measurements were performed on a Risø TL/OSL-DA 20 instrument with a $^{90}Sr/^{90}Y$ β-source that delivers a dose rate of 0.144 Gy s^{-1} to quartz coarse grains on stainless steel discs (Risø calibration quartz batches 71, 90, and 113). OSL signals were stimulated by an array of blue (470 ± 5 nm) LEDs with a nominal power density of 36 mW cm^{-2} for 38 s and collected by an EMI 9235QB15 photomultiplier tube with a 7.5 mm Hoya U340 glass filter in front of it. To establish the dose response curve (DRC), signals were integrated over the first 0.7 s of the decay curve and a background averaged from the last 2 s was subtracted. The DRC was fitted with a single saturating exponential function and the equivalent dose (D_e) determined through interpolation using the Analyst software (v3.24; Duller, 2015).

Preparatory tests were performed to determine the most suitable measurement parameters for D_e determination (e.g., Kim et al., 2009). Thus, dose recovery and preheat plateau tests (DRT and PPT, respectively) were carried out on 15 aliquots from three samples collected at 1.05 m deep in Pit 1, 1.40 m deep in Pit 2, and 2.05 m deep in Pit 4 (Fig. 2), testing the temperature range between 180 and 260 °C at 20 °C increments. For the DRTs, the natural signal was bleached in a Hönle UVACube for 30 min and samples were given a β-dose in the range of the natural dose. In addition to multi-grain measurements on 1 mm aliquots, single-grain analyses of 500 grains were performed for samples collected at 1.05 m deep in Pit 1 and 2.05 m deep in Pit 4.

Equivalent doses were determined on 40 to 48 aliquots per sample by applying the single-aliquot regeneration method (SAR; Murray and Wintle, 2000). Aliquots were accepted for age calculation if the recycling ratio was in the range of 0.9–1.1, recuperation rate was <5 %, and a test dose signal error was <10 %. Furthermore, the IR-depletion ratio test (Mauz and Lang, 2004) was applied to all measurements to assure the purity of quartz. For samples that displayed a scattered D_e distribution or considerable percentage of rejected aliquots, an additional set of 24 or 48 aliquots was measured to ensure a statistically valid dose determination. The central age model (CAM; Galbraith et al., 1999) and

minimum age model (MAM; Galbraith et al., 1999) were applied to all accepted D_e values via the R-package 'Luminescence' v0.9.10 (Kreutzer et al., 2012; R Core Team, 2021). The model parameter representing the overdispersion (σ_b) was estimated from the DRT.

3.3.2.3. Dose rate estimation. Present day water content was determined based on weight loss after drying samples at 40 °C and carbonate content was determined based on weight loss after dissolution in 10 % HCl. As of our understanding of the depositional environments, current moisture content does not reflect a representative value for the burial period, thus a higher water content of 10 ± 3 % was assigned to represent a former palustrine-lacustrine environment (Diaz et al., 2019).

The concentrations of U, Th and K were determined at Actlabs (Canada) via fusion inductively coupled plasma mass spectrometry (FUS-ICP-MS; Table 2). Current sample depth was considered to estimate the cosmic dose rate. The overall dose rates and luminescence ages were calculated with DRAC (v1.2; Durcan et al., 2015) using conversion factors from Guérin et al. (2011), α-attenuation factors from Brennan et al. (1991) and β-attenuation factors from Guérin et al. (2012).

4. Results

4.1. Lithological observations and particle-size distributions

Pits 1 and 2 are located on sand ridges, whereas Pits 3, 4, 5, and 6 on their margins (Fig. 2). The compilation of data from these localities is crucial for the understanding of the long-term development of the geomorphological features as well as to observe the temporal field relationships between the ridges and their surroundings (Fig. 3a, b).

The lithological logs are generalized to the dominant lithology and show a succession from silt-rich to sand-rich sediments, interbedded with sandy carbonate (Fig. 3a). Pit 1 (2.27 m deep) consists of a sandy carbonate layer of ~47 cm thickness appearing between two fine sand units, whereas Pit 2 (with a maximum depth of 1.30 m) consists of fine sands overlying a sandy carbonate layer. This pit is situated at the highest elevation, i.e., ~941 m. At Pit 3 (1.68 m deep), a sandy carbonate bed is overlain by fine sands. Sample H5P3 (Fig. 3a) contained amorphous siliceous aggregates and was not included in the end-member analysis to avoid inaccurate interpretation of the results. Pit 4 (2.2 m deep) and Pit 5 (2.18 m deep) are dominated by fine sands. Lastly, Pit 6 is positioned at the lowest elevation of ~935 m with a depth of 2 m and is dominated by fine sands in contact with silt-rich sediments at its bottom.

EMMA processing allowed four statistical sedimentary contributors (labeled EM1, 2, 3, and 4) to be identified (Fig. 4). The EM1 curve has a leptokurtic shape with a single mode in the sand fraction at 120 μm, corresponding to a very well sorted sand. In EM2, two distinct maxima are observed with a mode at 120 μm and the other at 250 μm, showing a mixing association of two sandy compartments. The EM3 curve displays a leptokurtic shape with a mode at 250 μm, emphasizing a very well sorted sand. Finally, EM4 has a leptokurtic shape with a mode at 250 μm and a minor platykurtic distribution centered in the silt fraction, around 15 μm (Fig. 4a). The weight of the distinctive EMs in each PSD allowed groups of samples to be sorted, underlying the prominent role of the sandy fractions, except when EM4 is present in a large proportion.

The sand ridge (Pits 1 and 2) is mainly characterized by EM2 in the bottom part, whereas the upper parts are comprised of EM1, EM3 and EM4 (Fig. 4b). This transition is clearly evident only on the sand ridge. On the other hand, the sand ridge margins are characterized by two
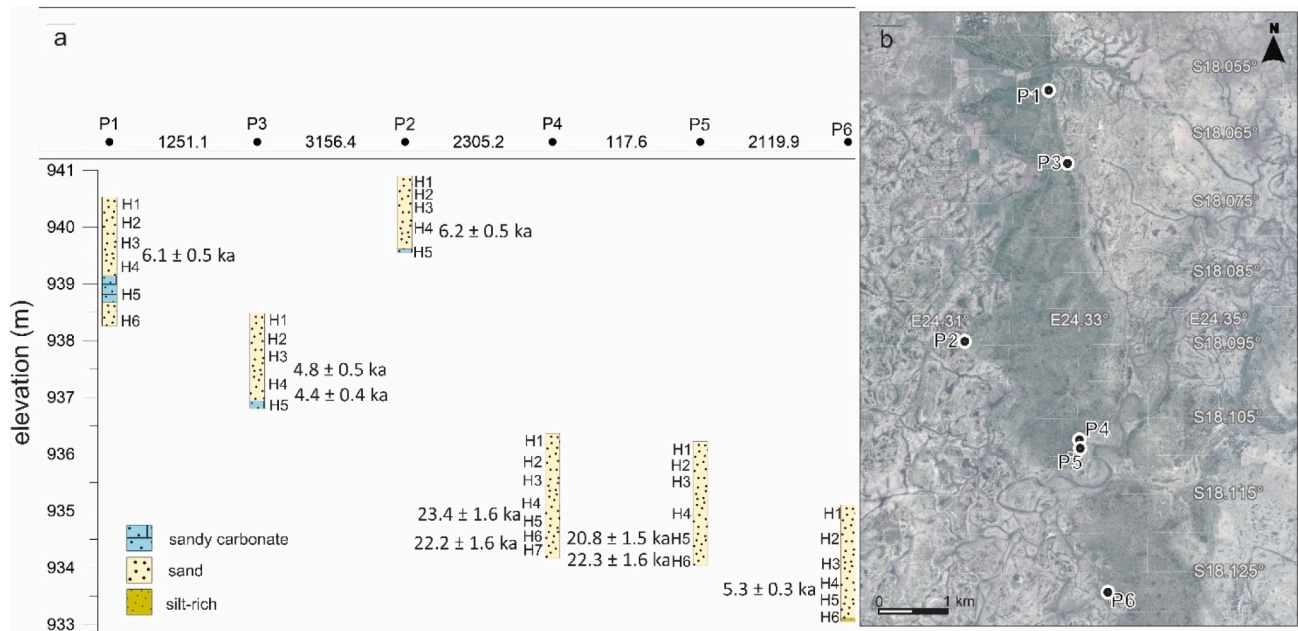
Table 2

Characteristics of the GPR profile lines considered in this study.

Profile line	Profile orientation	Profile length (m)	Time window (ns)	Number of stacks	Antennae separation (m)	Traces	Antenna frequency (MHz)
GPR-1	NE–SW	200	500	16	2.2	1697	100
GPR-2	NW–SE	220	500	16	2.2	1535	100

Fig. 3. (a) Lithological logs and corresponding OSL ages: classes are generalized from the particle size distribution analysis using the classification scheme by Folk (1954). Pit sites are denoted by P1 to P6. H1 to H6 refer to sample positions in each pit. Along the horizontal axis, figures between the pit numbers (P1 to P6) refer to the distance (in metres) between two successive pits from north to south. The y-axis refers to the altitude (in metres) at the top of the pit. (b) Locations of the pits referred to in (a). See also Fig. 2.
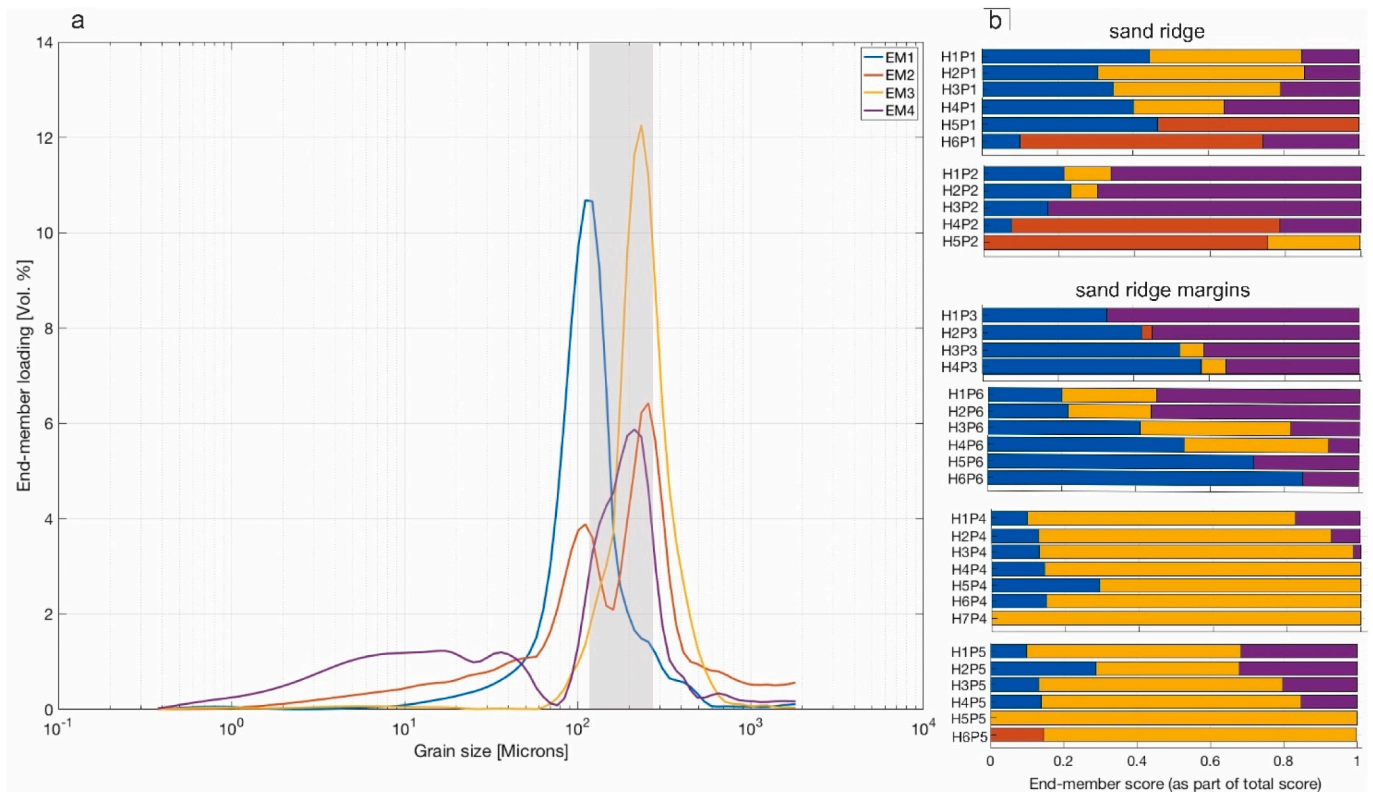

Fig. 4. (a) PSD plot of end-members determined via End-Member Mixing Analysis (EMMA). The Kalahari sand mode is displayed as a shaded area centred on 200 μm. (b) Bar chart of the end-member contributions to each sample.

distinct patterns. The first pattern, recognized in Pits 4 and 5, is dominated by EM3 and a minor contribution of EM1 and EM4 (Fig. 4b). EM3 represents very well sorted sand. The second pattern, observed in Pits 3 and 6, is mostly EM1 and EM4 with minor EM3 (Fig. 4a). Furthermore,

the transition in all sites is prominent, as the EMMA results (Fig. 4b) display a clear picture of evolution of the PSD for each site, from the sand ridge to its margins. This is an equally important step in emphasizing how end-members successfully characterize the variability of the

curves (Fig. 4), ultimately giving insight into possible sedimentary sources across the region.

4.2. Electrical resistivity tomography (ERT) profiles

All the ERT inversion results presented in this work correspond to the dipole-dipole electrode array configuration, which has improved lateral resolution characteristics compared to the Wenner-Schlumberger configuration (Loke, 2004). This made it easier in our interpretations to define the lateral distribution of sedimentary bodies.

4.2.1. Sand ridge

Profile ERT-1 is 214-m long and was acquired along the sand ridge in a NE–SW direction (Fig. 2a). The ERT inversion results for this profile (Fig. 5a) show a near-surface layer having increasing thickness towards the SW, whose resistivity values range between 200 and 4000 Ωm. This layer corresponds to moderately sorted fine sands observed in Pit 1 (Fig. 3a), where variations in resistivity are likely controlled by the amount of silt present. Below these fine sands, the resistivity values along the profile are seen to decrease (<100 Ωm), which we interpret as indicating a transition from fine sand to silt-rich floodplain deposits. Within these deposits, zones of increased resistivity can be observed on the left-hand side of the profile, which may represent paleo-channels consisting of fine sand. These channels are located between approximately 8 and 20 m depth.

Profile ERT-2 was acquired across the sand ridge in a NE–SW direction (Fig. 2b). Similarly, the corresponding ERT inversion results (Fig. 5b) show a relatively resistive layer at the top overlying a dominant conductive layer of values <100 Ωm. However, the upper layer is discontinuous with the middle section showing zones we interpret as paleo-channels closer to the surface. Our interpretation of this profile (Fig. 5b) shows a fine sand layer overlying silt-rich floodplain deposits, with an eroded surface from 30 to 112 m. Paleo-channels can be identified within the floodplain at a depth of approximately 2 to 5 m.

4.2.2. Sand ridge margins

The sand ridge margins correspond to a transition between the floodplain and the sand ridge. Profile ERT-3 is situated on the eastern margin of the sand ridge in the southern part of the study area (Fig. 2a). The corresponding ERT inversion results (Fig. 6a) show a more resistive layer at the surface from approximately 30 m onwards, whose thickness increases towards the west. This layer has been identified as fine sand in Pit 3 (Fig. 3a). Below the fine sand, is a section dominated by a conductive layer of values ~20 to ~100 Ωm, corresponding to the silt-rich sediments of the floodplain. Within this conductive floodplain, a relatively resistive feature is displayed and interpreted as a paleo-channel. Profile ERT-4 crosses the sand ridge margin from N to S (Fig. 2b). Here, the ERT inversion results (Fig. 6b) again show a resistive upper layer, representing fine sand, overlying a more conductive layer corresponding to silt-rich sediments observed in Pit 4 (Fig. 3a). Likewise,
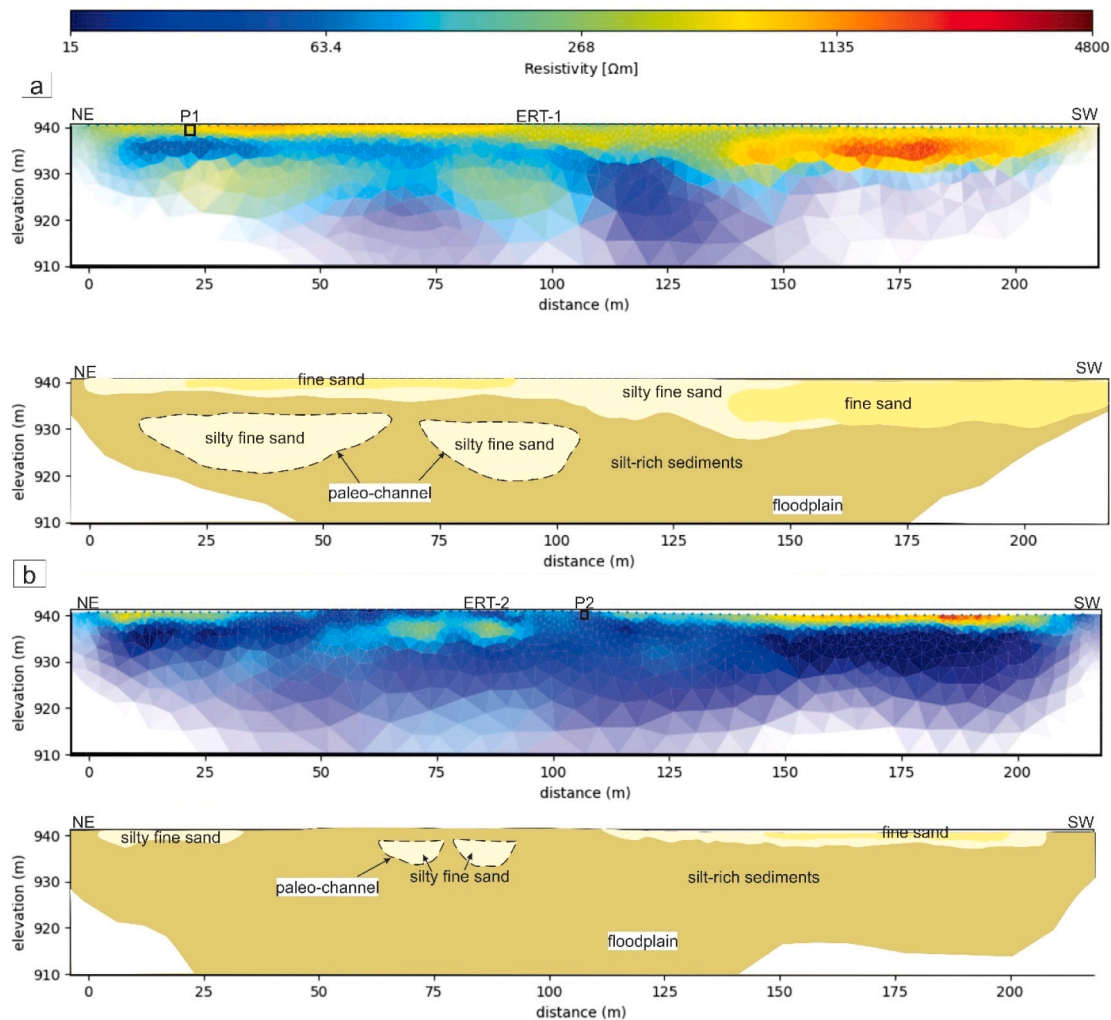

Fig. 5. Dipole-dipole ERT profiles (a) ERT-1, and (b) ERT-2, which were acquired along the sand ridge (Fig. 2). Shown are the inversion results and their interpretations based on the observed resistivity values and sedimentological data.
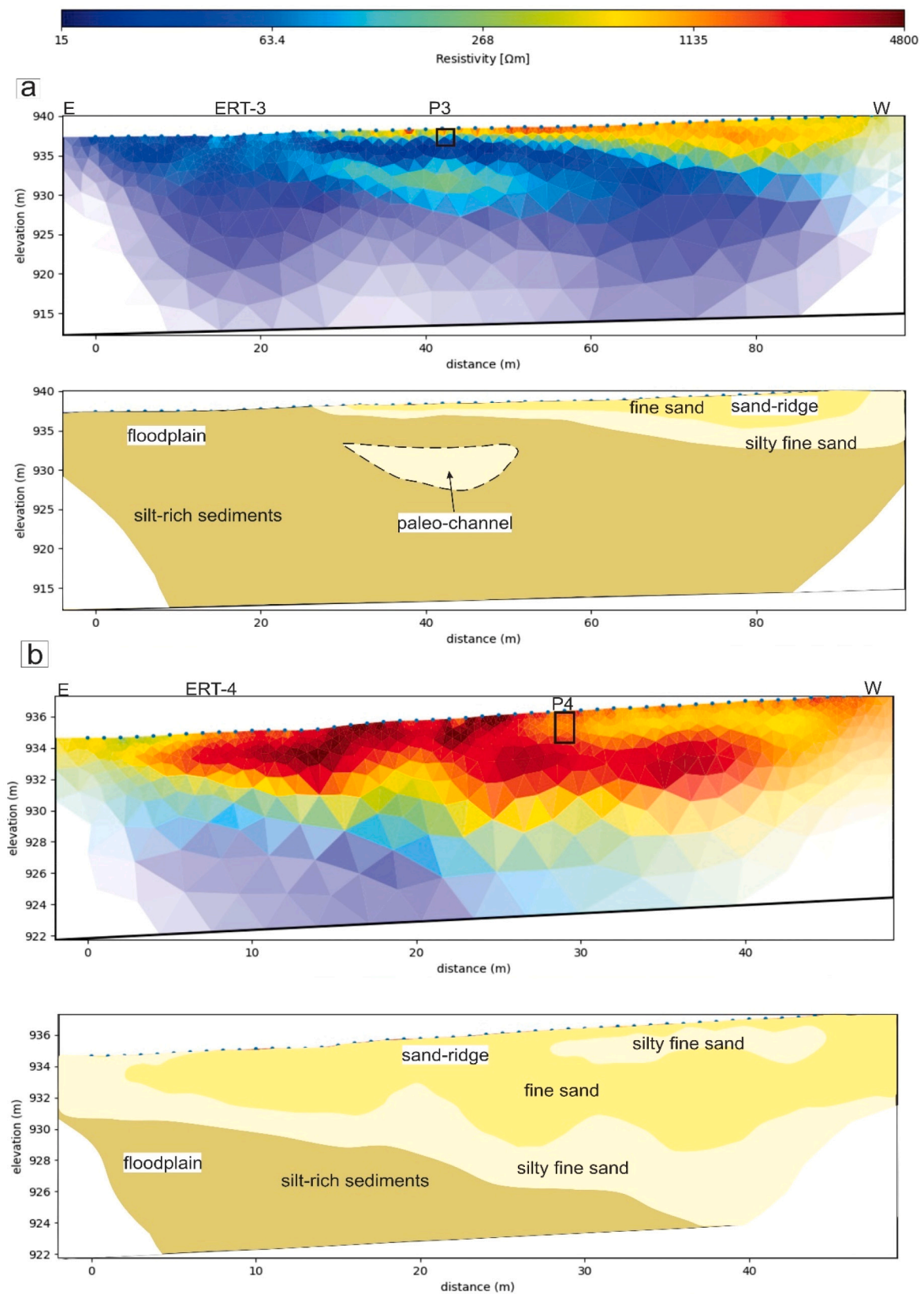
Fig. 6. Dipole-dipole ERT profiles (a) ERT-3 and (b) ERT-4 across sand ridge margins (Fig. 2). Shown are the inversion results and their interpretations based on the observed resistivity values and sedimentological data.

Profile ERT-5 runs across a sand ridge margin dominated by a resistive layer (>200 Ωm) from 20 to 47 m, which corresponds to fine sand in Pit 5 (Fig. 3a). The fine sand is underlain by a more conductive layer (<70 Ωm) representing silt-rich sediments of the floodplain. Finally, profile ERT-6 (Fig. 2c) runs along the N–S trending sand ridge margin in the southern part of the study area. The ERT inversion results (Fig. 7b) show consistency with previously presented data having a more resistive upper layer with values >600 Ωm (fine sand), and a relatively conductive lower layer (<60 Ωm) corresponding to silt-rich sediments of the floodplain below Pit 6 (Fig. 3a). It is important to note that the conductivity will vary depending on the moisture or clay content of the floodplain sediments.

4.3. Ground-penetrating radar (GPR) profiles

Profile GPR-1 is 200-m long and was acquired along the sand ridge in a NE–SW direction (Fig. 2a). The GPR results (Fig. 8a) show two continuous reflectors at approximately 2 to 4 m depth. The upper reflector terminates on the lower one, revealing the internal structure and relative chronology (Bristow and Jol, 2003) within the ridge. Profile GPR-2 is 220-m long and was acquired along the sand ridge in a NW–SE direction (Fig. 2b). Similarly, the GPR results (Fig. 8b) show two continuous reflectors running subparallel to the ground surface, each occurring between depths of ~2 to ~4 m and ~6 to ~8 m. The lower reflector occurs closer to the boundary of high signal attenuation hence appearing less continuous. Diffraction hyperbolae appearing on both profiles at an apparent depth of ~7 to 10 m are caused by trees along the survey line. The maximum GPR penetration depth along these profiles is approximately 12 m.

The Chobe Enclave sand ridges are thus characterized by prominent continuous reflectors consistent throughout the area with varying thickness, whereas the surrounding floodplains show high signal attenuation because of their increased fine sediments and/or moisture content. The interpreted models (Fig. 8a, b) emphasize some continuous bounding surfaces, characterized by continuous reflectors along the sand ridge, and a transition zone, defined by a boundary of high signal attenuation. Generally, this is consistent with the ERT inversion results showing a transition between the resistive sand ridge and the conductive silt-rich floodplain.

4.4. Optically stimulated luminescence (OSL) results

All processed samples were dry with <0.5 % water content (except for OP5-103 with <2 % water) and contained neglectable amount of carbonate and feldspar (Table 3). Preheat plateau tests (PPT) imply that a preheat temperature of 200 °C is collectively best suited for all samples (Fig. 9); this temperature along with a cut heat to 200 °C was utilized during D_e measurements. Dose recovery tests (DRT) carried out with this preheat temperature resulted in dose reproducibility within 4 %, 2 %, and 1 % for samples OP1-105, OP2-140, and OP4-205, respectively. D_e values from single-grain measurements are indistinguishable (within error) for sample OP1-105 and higher by 4 % for sample OP4-205 than the multi-grain D_e (Fig. 9). Central age model (CAM) and minimum age model (MAM) results in pits 2, 4, and 6 agree within 1σ uncertainty. In pits 1, 3, and 5, over 40 % of variance subsists between CAM and MAM, and CAM ages are presented (Table 3).

The effects of inter-grain variability in the degree of bleaching, β micro-dosimetry effects, bioturbation, and grain-to-grain differences in OSL characteristics for an analogous set of samples were discussed in Burrough et al. (2009). These authors concluded that the most suitable age model for this type of sediment is the CAM. They also estimated the internal activities of ^{238}U, ^{232}Th, and ^{40}K within the quartz grains, showing that the internal α- and β-dose would not push the age estimates outside of the assigned 1σ uncertainties and would not affect age clusters calculated subsequently. Therefore, CAM ages were calculated based on the dose rate estimated from the radioelement concentrations measured

within bulk samples and the corresponding cosmic dose. The resultant ages are in stratigraphic order within 1σ uncertainties and are clustered into two age groups that range between 23.4 ka and 20.8 ka and between 6.2 ka and 4.4 ka. The older age group is found between 2.1 m and 1.7 m depths in pits 4 and 6 while in pits 1, 2, 3, and 5, where maximal sampling depth is 1.4 m, samples display a Holocene age.

5. Discussion

5.1. Geometry and internal structures of landforms

5.1.1. The sand ridge

The remnant asymmetrical and linear morphology of sand ridges in the Chobe Enclave remains sparsely vegetated with elevations reaching as high as 936 m (Fig. 1d). Secondly, the eastern margins of individual ridges show a sharp linear contact with the floodplain, whereas their western margins display typical *en-chevron* shapes (Fig. 2). This geometry is the consequence of sheetwash erosion on slopes of asymmetrical structural reliefs in arid and semiarid zones (Parsons and Abrahams, 2009), the longest slope dipping into the direction of the open *en-chevron V*-shape (Fig. 1). Nevertheless, some steep slopes enclose these geomorphological features (Fig. 1e), emphasizing some inheritance: indeed, the sand-ridge appears as a fossil relief, shaped in a different environment than at present, in order to get the *en-chevron* morphology. Today, however, erosion seems to equally affect both sides of the ridge (Fig. 1d). Moreover, the Chobe Enclave sand ridges have been formerly reported as floodplain beach ridges that were emplaced synchronously with Lake Thamalakane phases (Burrough and Thomas, 2008). Typically, beach ridges refer to stabilized, aeolian, relict wave-built shoreline features, which may consist of either siliciclastic or calcareous clastic material. Before they were stabilized, they would either have a regressive or transgressive history (Otvos, 2000). On the other hand, the internal structure of sand ridges from GPR profiles indicates the presence of bounding surfaces (Fig. 8), emphasized by continuous sub-horizontal reflectors. These internal structures suggest the past occurrence of *different depositional events within the ridges*. The processed GPR reflection data allowed the internal structure of the sand ridge to be observed to a depth of 8 m and prominent radar surfaces were identified as continuous bounding surface (*cbs*). Below these features, there is a boundary of high signal attenuation, indicating a finer conductive unit below or a zone of higher moisture content. This latter could represent the floodplain deposits or finer sediments with higher moisture content. The *cbs* correspond to possible *erosional bounding surfaces* and are characterized by continuous sub-horizontal reflectors along the sand ridge. From the above evidence, the internal structure of the sand ridge likely relates to a transition zone from the upper dry sand with erosional surfaces to lower floodplain deposits/finer sediments with high moisture content. Consequently, the erosional bounding surfaces observed in the deep parts of the sand ridge could originate either from a lacustrine (associated to shore erosion due to paleo-lakes) or an aeolian environment, or a result of both.

Furthermore, there are different sedimentary sources identified corresponding to specific origins found in the landscape of the Chobe Enclave from the interpretation of the EMMA of the PSD data. The main sedimentary sources from different bodies can be mixed in various proportions (Van Thuyne et al., 2021). Results from the *sand ridge and its margins* show similar groups of grain size contributors, but with distinct variations individually. The Kalahari sands constitute the prominent sedimentary source, characterized by the modes centered around 200 μm (Mokatse et al., 2022 and references therein) and corresponding to EM3 (Fig. 4a, b). This source has endured different phases of erosion and reworking with different proportions observed across study sites (Fig. 4b). Another depositional phase of the Kalahari sand is noted on the sand ridge margins, where two age clusters are observed (Fig. 4b). The first one shows the presence of the Kalahari sand, dominant in Pits 4 and 5 and represented by EM3, with ages ranging from 23.4 to 20.8 ka. The
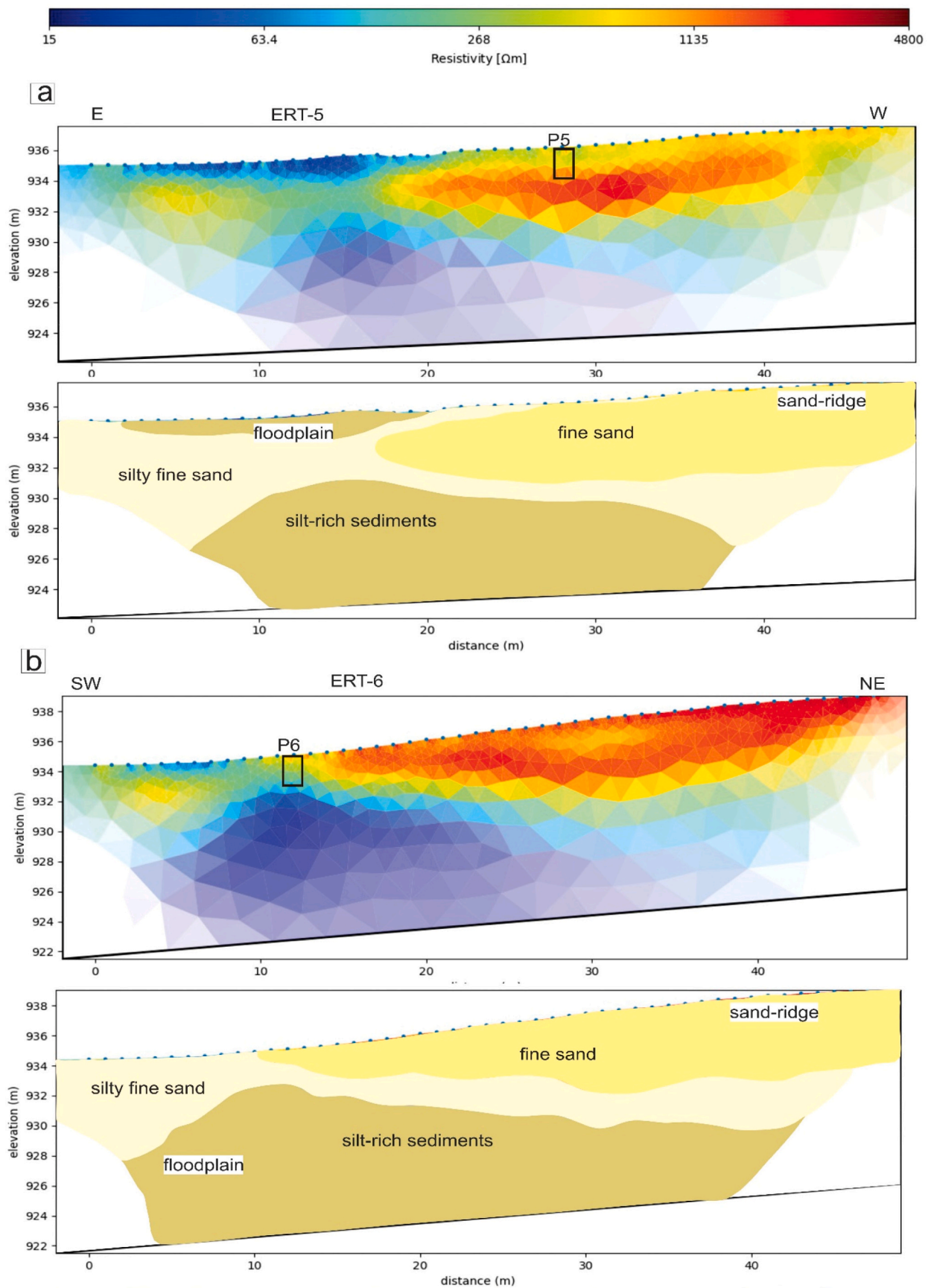
Fig. 7. Dipole-dipole ERT profiles (a) ERT-5 and (b) ERT-6 across sand ridge margins (Fig. 2). Shown are the inversion results and their interpretations based on the observed resistivity values and sedimentological data.
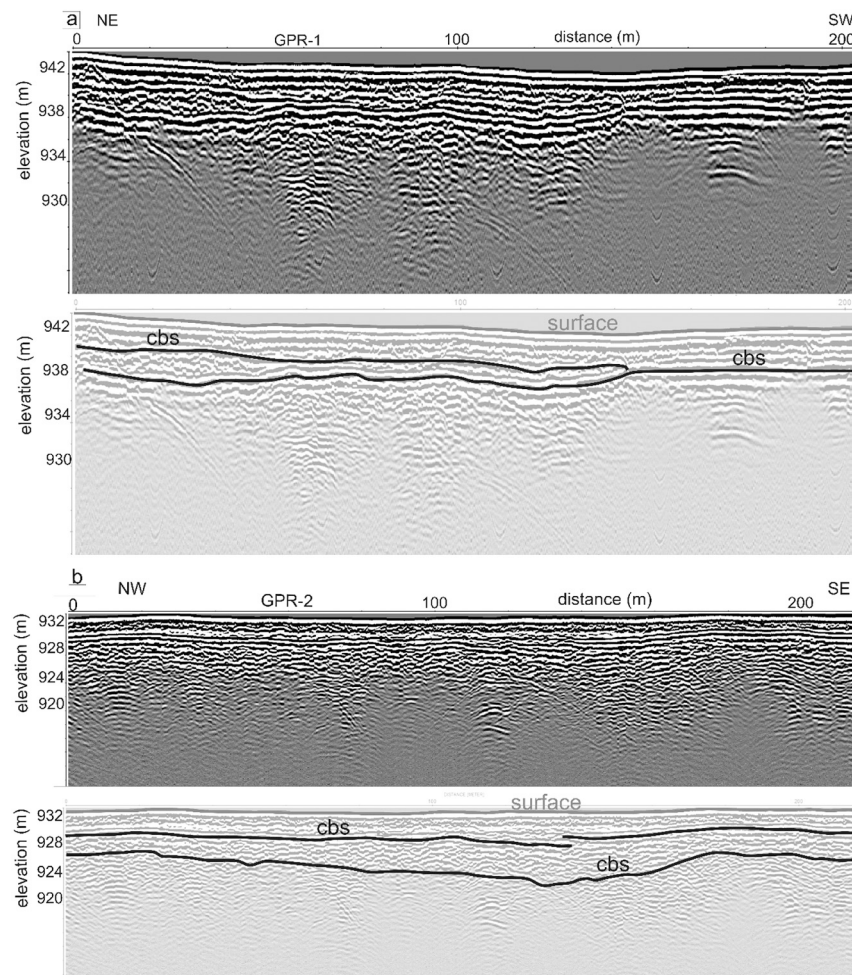
Fig. 8. GPR profiles (a) GPR-1, and (b) GPR-2, which were acquired along the sand ridge (Fig. 2). Shown are the processed 100-MHz reflection data and their interpretations. (cbs = continuous bounding surface).

second cluster shows a larger contribution of EM1 and EM4 with ages ranging from 5.3 to 4.4 ka. The sediments from these sites include a proportion of reworked Kalahari sands, desert loess, and a diatomite mud fraction (Van Thuyne et al., 2021). EM4 displays the platykurtic curve of diatomite mud with the influence of a desert loess fraction. The last depositional phase observed occurred on the sand ridge, displaying the onset of EM2 at the bottom, and contribution of EM1 and EM4 at the top (Fig. 4b). It is evident that EM2 is particularly distinct on the sand ridge with ages ranging from 6.2 to 6.1 ka. The occurrence of EM2 on the sand ridge marks the deposition of reworked material of EM3 and EM1. The sand ridge and its margins compose of a mixture of one or more grain size signatures, each corresponding to a specific source. Consequently, it is revealed that the Kalahari sands (EM3) constitute the parental material of the coarse fraction dominating on the sand ridge margins. On the other hand, the sand ridge margins show a transition to a dominant presence of fine sand (EM1) and diatomite mud (EM4). Lastly, a mixture of Kalahari sands and fine sand demonstrated by EM2 thrives on sand ridges with an increased reworking of Kalahari sand, diatomite mud, and fine sand on the upper portions of the ridges.

5.1.2. The floodplain

The spatial distribution of the various lithologies was assessed using ERT, which showed the presence of resistive units within floodplain deposits that we interpret as evidence of *paleo-channels* (Figs. 5 to 7). Indeed, these features likely correspond to silty fine sand bodies within the conductive silt-rich floodplain sediments. Most of the Chobe Enclave landscape is occupied by the floodplain undergoing aeolian and fluvial

dynamics (Mokatse et al., 2022), and its extent limits are bounded by the Chobe and Linyanti faults. However, the sand ridge overlying the floodplain deposits displays quite astonishing features on its margins with the floodplain. These are the sharp linear contact on eastern margins and *en-chevron* patterns on the western margins. Moreover, one key feature is the antecedent drainage pattern cutting through the sand ridges (a watergap), an identification of a tectonically controlled geomorphological feature.

5.2. The suspected role of neotectonic activity

The present-day entrenched and anastomosed fluvial system (Fig. 1b, c) suggests that fluvial deflection in the Chobe is controlled by epeirogenic movements (Holbrook and Schumm, 1999). Indeed, the deflection of channels into the sagging basin, that is illustrated to have happened in the past by the presence of the paleo-channels revealed in this work, implies subsidence within the flanking structural highs. As it typically occurs in low-relief areas that experience a discrete topographical disturbance, deflection of a river during an uplift or into a zone of subsidence will manifest as an abrupt shift in the river course coincident with the deformed zone (Holbrook and Schumm, 1999). This is observed in the Chobe Enclave, where *fluvial watergaps* cut through sand ridges (Fig. 1b, c). Such features, observed at lower elevations are typical geomorphological indicators that usually attributes for a neotectonically influenced landscape (Clark, 1989). Furthermore, the *en-chevron* morphology displayed on the western margins and sharp linear contact on the eastern margins of the sand ridge in the Chobe Enclave are similar

Table 3
OSL ages of the studied samples, based on the central age model (CAM).

Sample	Pit no	Depth [cm]	Accepted/ measured aliquots	K [wt%]	1σ	Th [ppm]	1σ	U [ppm]	1σ	CaCO₃ [wt%]	Measured H₂O [wt%]	Estimated H₂O [wt%]	Dose rate [Gy ka⁻¹]	1σ	D_e [Gy]	1σ	Overdispersion [%]	1σ	Age [ka]	1σ
OP1-105	P1	105	35/35	0.06	0.01	0.6	0.08	0.4	0.02	1.6	0.1	10	0.372	3	2.26	0.022	0.13	35	4	6.1	0.5
OP2-140	P6	140	46/46	0.07	0.01	1.0	0.14	0.3	0.02	0.0	0.1	10	0.377	3	2.00	0.022	0.03	9	1	5.3	0.3
OP3-105	P3	105	78/94	0.09	0.01	0.8	0.11	0.3	0.02	1.2	0.3	10	0.390	3	1.89	0.022	0.15	66	6	4.8	0.5
OP3-120	P3	120	73/81	0.09	0.01	0.8	0.11	0.3	0.02	5.1	0.5	10	0.387	3	1.69	0.022	0.13	70	6	4.4	0.4
OP4-185	P4	185	43/47	0.06	0.01	0.6	0.08	0.2	0.01	0.0	0.0	10	0.314	3	7.35	0.020	0.18	15	2	23.4	1.6
OP4-205	P4	205	48/48	0.02	0.00	0.3	0.04	0.2	0.01	0.0	0.0	10	0.256	3	5.67	0.018	0.12	14	2	22.2	1.6
OP5-103	P2	103	43/48	0.13	0.02	0.8	0.11	0.2	0.01	1.8	1.7	10	0.406	3	2.50	0.025	0.14	35	4	6.2	0.5
OP6-170	P5	170	65/70	0.03	0.00	0.4	0.06	0.2	0.01	0.0	0.0	10	0.278	3	5.78	0.019	0.12	19	2	20.8	1.5
OP6-210	P5	210	58/72	0.03	0.00	0.4	0.06	0.2	0.01	0.0	0.0	10	0.270	3	6.02	0.019	0.15	20	2	22.3	1.6

features to those observed on the Magikwe ridge (Burrough and Thomas, 2008, their Fig. 2) in the tilted Mababe basin (Gumbricht et al., 2001), with both Magikwe ridge and the Chobe Enclave sand ridge being incised by *fluvial watergaps*. Although small-scale neotectonic activity is not easily visible, GPR imaging of the subsurface and OSL dating of the sand ridges and sand ridge margins suggest some tectonic uplift. The resultant ages showed two clusters corresponding to the sand ridges and sand ridge margins, respectively. On the sand ridges, Pits 1 and 2 display consistent ages between 6.1 ± 0.5 and 6.2 ± 0.5 ka (Fig. 3a), whereas on the sand ridge margins there are two recognizable age sub-clusters. The first cluster observed in Pits 4 and 5 provides late Pleistocene ages from 20.8 ± 1.5 to 23.4 ± 1.6 ka and the second, in Pits 3 and 6, Holocene ages from 4.4 ± 0.4 to 5.3 ± 0.3 ka (Fig. 3a). In addition, the synde-positional uplift of the ridge is further evidenced by the presence of erosional bounding surfaces. Geochronology of the sand ridge and sand ridge margins is further supported by the PSD curves using end-member contributions (Fig. 4a). Specifically, on the sand ridge, which is evidently dominated by the contribution of EM2, it is the only site with this signature. This observation possibly links the onset of EM2 on the sand ridge with the syndepositional uplift event. These observations must reflect the deformation caused by epeirogenic movements acting on the low relief landscape of the Chobe Enclave at the time. Indeed, the topographic positions of studied pits and their corresponding sedimentary signatures show evidence of variability of sediments because of erosion. The sedimentary signatures from end-member contributions in the PSD support this as well, due to the reworking of sediments. This strongly suggests that an erosional phase could have been triggered by a possible neotectonic activity, the latter providing some relief potential for sediment reworking and erosion in this otherwise very flat topography.

The development of the large-scale Chobe Enclave landscape is hypothesized to have begun with high displacement rate along the Chobe fault (Alvarez Naranjo, 2016). The Chobe fault is considered as the main border fault of the Okavango Graben; its nucleation points on the surface and its propagation direction along strike is NE–SW (Kinabo et al., 2008; Alvarez Naranjo, 2016). This configuration (zone of high displacement) resulted in a depocenter forming the Chobe-Linyanti sub-basin (Kinabo et al., 2007), where the formation of sharp linear eastern margin of the sand ridge indicative of wet (lake shoreline?) conditions likely began because of the subsidence of the Chobe fault hanging wall (Fig. 10). At this time, the subsidence of the Chobe fault hanging wall resulted in burial of a distributary channel system, observed as paleo-channels in this study. Evidence for fault segments linkage of Linyanti fault confirms its development (Kinabo et al., 2008), this resulting in uplift of the footwall and erosion. This ultimately triggers the erosion on the western margins of the sand ridge found in the Chobe Enclave and giving rise to the development of the current landscape.

5.3. Evolution of depositional environments and Chobe Enclave's landscape

The Middle Kalahari paleolake system has been a major component for understanding late Quaternary climate and hydrological dynamics. The existence of a megalake system was proposed due to a consistency in ridge altitudes within basins of this system, with major lake highstands identified from OSL dating (Burrough et al., 2009, their Fig. 4). According to Burrough et al. (2009), the paleolacustrine environment gave rise to paleolake shorelines common to the western margins of the basins. The 'wave-built' shorelines on the western margins of paleolake Makgadikgadi are considered to be constructed by an easterly wind component of the climate system. However, it is first necessary to state that the landscape formation of the Chobe Enclave occurred in an environment situated between two faults (Linyanti and Chobe), where linkages between fault segments have prevailed and proven to exert profound influence on development of neotectonics and fluvial activities. Consequently, the drainage patterns of the fluvial systems in the
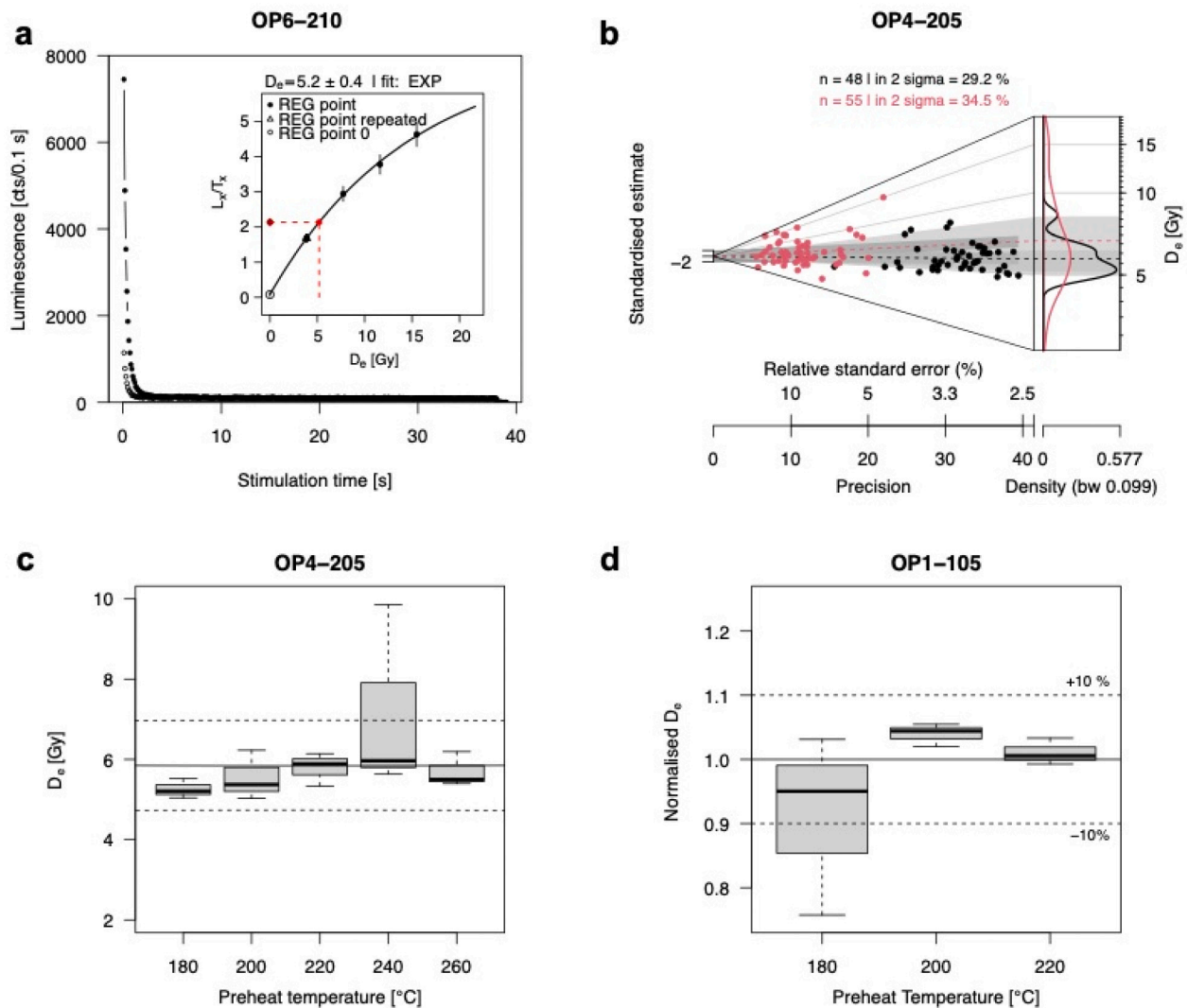
Fig. 9. Luminescence characteristics of the analysed quartz samples from the Chobe enclave. (a) OSL decay curves of one aliquot of sample OP6-210. Solid symbols denote the natural decay curve; open symbols represent the decay curve corresponding to the first test dose. The inset shows a representative dose response curve of the same sample, fitted with a single saturating exponential function. (b) Abanico plot (Dietze et al., 2016) of the multi-grain (black) and single-grain (red) D_e distributions of sample OP4-205 (weighted mean as central value). (c) Boxplot of the preheat plateau test results of sample OP4-205. Three aliquots were analysed for each preheat temperature. The solid black line marks the average dose of all shown aliquots (5.85 Gy); the dashed lines represent the standard deviation from this value. (d) Boxplot of the dose recovery test results of sample OP1-105. The recovery dose administered was 2.15 Gy. Three aliquots were analysed for each preheat temperature.

Chobe Enclave, and this part of the Middle Kalahari, were certainly influenced by these fault zones, their linkage between these zones, and the preexisting basement fabrics (Kinabo et al., 2008). This was undoubtedly a factor controlling the Late Pleistocene to Holocene landscape in the Chobe Enclave.

The evolution of the region (Fig. 10) can be summarized as follows: (1) the propagation of the NE–SW trending Chobe fault resulted in high displacement along the fault. Before ~25 ka (Fig. 10a), the fluvial systems endured burial of channels with continuous deposition across the landscape. Silty fine sand paleo-channels formed within the silt-rich floodplain deposits overlain by fine sand of the ridges. The sizes of the paleo-channels varied depending on their probable depositional patterns (Fig. 10a). These depositional patterns were the result of fluvial deflection due to epeirogenic movements (Holbrook and Schumm, 1999). (2) During a second step of neotectonic uplift events, between ~25 and ~6 ka (Fig. 10b), syntectonic deposition occurred and the continued propagation of the Chobe fault formed a depocenter making part of the Chobe-Linyanti sub-basin (Kinabo et al., 2007). During this time, some sand ridges formed. This syndepositional uplift of the sand

ridge morphologies is attested by the presence of erosional bounding surfaces. This configuration triggered the formation of sharp linear eastern margin of the sand ridge, also representing a possible paleo-lake/marsh shore. Moreover, during this period, there is a prominent continued erosional phase, revealing the existence of carbonate islands emerging from the floodplain areas and creating a topographical inversion relief within the basin (Mokatse et al., 2022). Indeed, the presence of these palustrine carbonates refers to periods and/or areas of reduced clastic input and may be used as an indicator of the aggradation rate at work in the floodplain (Alonso-Zarza, 2003), as well as a change in the water chemistry. The carbonate precipitation events in the Chobe Enclave occurred irregularly, since at least ~75 ka (Diaz et al., 2019; Mokatse et al., 2022); they witness changes and some disorganization in the hydrological network, probably associated with phases triggered by neotectonics, although some climate influence cannot be totally discarded. Nevertheless, it is certainly during this phase, between ~25 and ~6 ka, that the watergaps started to form. (3) Finally, from ~6 ka to present day (Fig. 10c), continued fault growth and propagation of the Linyanti fault resulted in uplift of the footwall, which induced erosion to
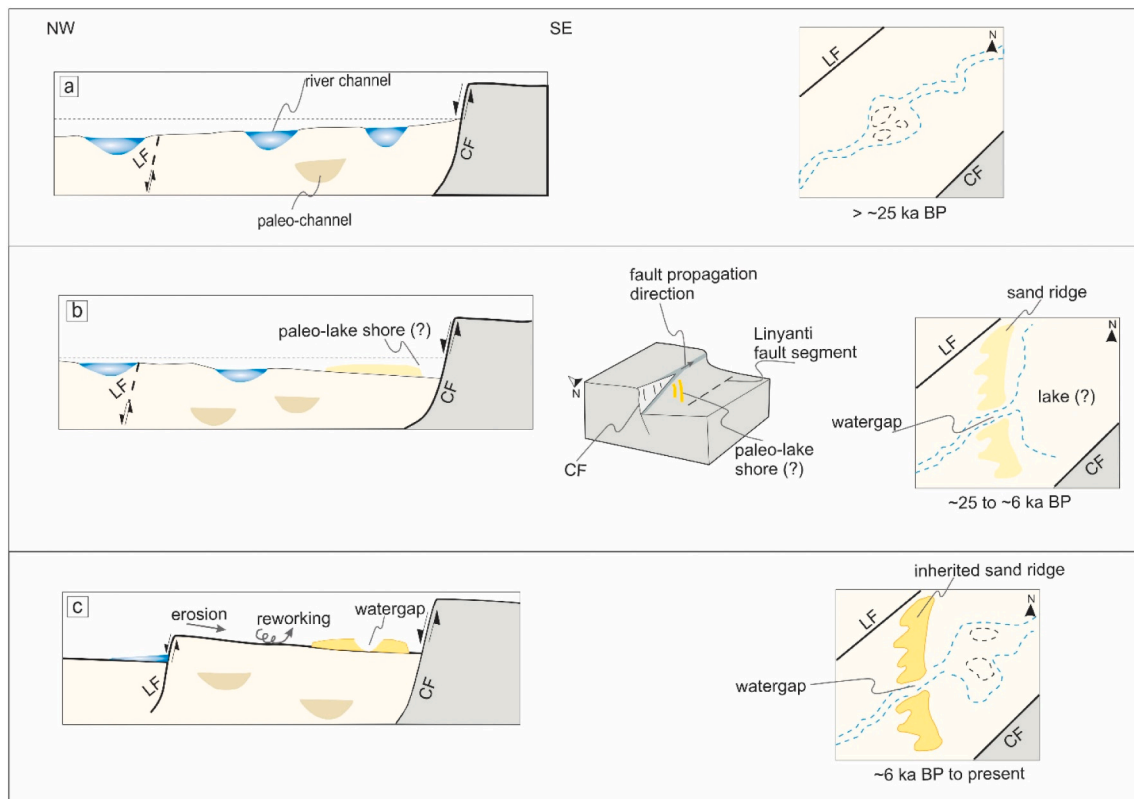
Fig. 10. Schematic diagram illustrating the landscape evolution of the Chobe Enclave during the Late Pleistocene to Holocene (for details see text). LF — Linyanti fault, CF — Chobe fault.

the NE of the Chobe Enclave. This contributed to essentially erode the western margins of the present-day sand ridge as well and deepen the fluvial watergaps. The sand ridge was progressively isolated from the floodplain level and constitutes an inherited relief, presently eroded on both of its flanks, due to aeolian and fluvial reworking as a continuous phase of the landscape shaping.

6. Conclusions

A combination of ERT, GPR, OSL, and sedimentological data was used to investigate the geometry, internal structure, and history of the Chobe Enclave's landforms. Different depositional environments were recorded during the Late Pleistocene to Holocene in the Chobe Enclave. Throughout this time, the reworking and deposition allowed the Kalahari sand to be mixed with various proportions of different sedimentary sources from desert loess to diatomite mud. The Late Pleistocene (>~25 ka) is characterized by burial of fluvial channels due to epeirogenic movements revealed as paleo-channels today. During ~25 ka to ~6 ka, a hypothetical paleo-lake shoreline formed, resulting in the linear eastern margin of the sand ridge. Furthermore, since ~6 ka, the neotectonic influence on the evolution of the landscape and drainage is attested by the incision of the sand ridge, forming fluvial watergaps. As this study gives insight on possible influence of neotectonics on the landscape, further work is needed to validate and explore the extent of neotectonics as well as development of the eastern-most sand ridges in the Chobe Enclave.

Declaration of competing interest

Eric P. Verrecchia reports financial support was provided by Swiss National Science Foundation.

References

Aitken, M.J., 1998. An Introduction to Optical Dating. The Dating of Quaternary Sediments by the Use of Photon-stimulated Luminescence. In: Oxford University Press, Oxford, New York, Tokyo, p. 267 pp..

Alonso-Zarza, A.M., 2003. Palaeoenvironmental significance of palustrine carbonates and calcretes in the geological record. Earth Sci. Rev. 60 (3–4), 261–298.

Alvarez Naranjo, A., 2016. The Role of Pre-existing Basement Fabrics in the Initiation of Continental Rifting: The Okavango Rift Zone, Botswana. Doctoral Dissertations, 2642. https://scholarsmine.mst.edu/doctoral_dissertations/2642.

Alvarez Naranjo, A., Hogan, J.P., 2013. The role of tectonic inheritance in the geometry and location of continental rifts-an example from the Okavango Rift Zone, Botswana. Geol. Soc. Am. Abstr. Programs 45 (7), 832.

Annan, A.P., Davis, J.L., 1992. Design and development of a digital ground penetrating radar system. In: Pilon, J. (Ed.), GroundPenetrating Radar. Geol. Surv. Can. Pap, 90-4, pp. 15–23.

Baines, D., Smith, D.G., Froese, D.G., Bauman, P., Nimeck, G., 2002. Electrical resistivity ground imaging (ERGI): a new tool for mapping the lithology and geometry of channel-belts and valley-fills. Sedimentology 49 (3), 441–449.

Barber, D.C., Brown, B.H., 1984. Applied potential tomography. J. Phys. E: Sci. Instrum. 17 (9), 723–733.

Bishop, M.P., Shroder Jr., J.F., Colby, J.D., 2003. Remote sensing and geomorphometry for studying relief production in high mountains. Geomorphology 55 (1–4), 345–361.

Brennan, B.J., Lyons, R.G., Phillips, S.W., 1991. Attenuation of alpha particle track dose for spherical grains. Int. J. Radiat. Appl. Instrum. Part D 18 (1–2), 249–253.

Bristow, C.S., 2009. Ground penetrating radar in aeolian dune sands. In: Jol, H.M. (Ed.), Ground Penetrating Radar: Theory and Applications. Elsevier Science, Amsterdam, The Netherlands, pp. 273–297.

Bristow, C.S., Duller, G.A.T., Lancaster, N., 2007. Age and dynamics of linear dunes in the Namib Desert. Geology 35 (6), 555–558.

Bristow, C.S., Jol, H.M., 2003. An introduction to ground penetrating radar (GPR) in sediments. Geol. Soc. Lond., Spec. Publ. 211 (1), 1–7.

Bristow, C.S., Lancaster, N., Duller, G.A.T., 2005. Combining ground penetrating radar surveys and optical dating to determine dune migration in Namibia. J. Geol. Soc. 162 (2), 315–321.

Bufford, K.M., Atekwana, E.A., Abdelsalam, M.G., Shemang, E., Atekwana, E.A., Mickus, K., Molwalefhe, L., 2012. Geometry and faults tectonic activity of the Okavango Rift Zone, Botswana: evidence from magnetotelluric and electrical resistivity tomography imaging. J. Afr. Earth Sci. 65, 61–71.

Burke, K., Gunnell, Y., 2008. The african erosion surface: a continental-scale synthesis of geomorphology, tectonics, and environmental change over the past 180 million years (Vol. 201). Mem. Geol. Soc. Am. 201, 1–66.

Burrough, S.L., Thomas, D.S., Shaw, P.A., Bailey, R.M., 2007. Multiphase quaternary highstands at lake Ngami, Kalahari, northern Botswana. Palaeogeogr. Palaeoclimatol. Palaeoecol. 253 (3–4), 280–299.

Burrough, S.L., Thomas, D.S.G., 2008. Late Quaternary lake-level fluctuations in the Mababe Depression: Middle Kalahari palaeolakes and the role of Zambezi inflows. Quat. Res. 69 (3), 388–403.

Burrough, S.L., Thomas, D.S., Singarayer, J.S., 2009. Late Quaternary hydrological dynamics in the Middle Kalahari: forcing and feedbacks. Earth Sci. Rev. 96 (4), 313–326.

Campbell, G., Johnson, S., Bakaya, T., Kumar, H., Nsatsi, J., 2006. Airborne geophysical mapping of aquifer water quality and structural controls in the lower Okavango DeltaBotswana. South African Journal of Geology 109 (4), 475–494.

Chorowicz, J., 2005. The East African rift system. J. Afr. Earth Sci. 43 (1–3), 379–410.

Clark, G.M., 1989. Central and southern Appalachian water and wind gap origins: review and new data. Geomorphology 2 (1–3), 209–232.

Cooke, H.J., 1980. Landform evolution in the context of climatic change and neo-tectonism in the Middle Kalahari of north-Central Botswana. Trans. Inst. Br. Geogr. 5 (1), 80–99.

Daly, M.C., Green, P., Watts, A.B., Davies, O., Chibesakunda, F., Walker, R., 2020. Tectonics and landscape of the Central African Plateau and their implications for a propagating Southwestern Rift in Africa. Geochem. Geophys. Geosyst. 21 (6), e2019GC008746.

Diaz, N., Armitage, S.J., Verrecchia, E.P., Herman, F., 2019. OSL dating of a carbonate island in the Chobe Enclave, NW Botswana. Quat. Geochronol. 49, 172–176.

Dietze, E., Hartmann, K., Diekmann, B., IJmker, J., Lehmkuhl, F., Opitz, S., Borchers, A., 2012. An end-member algorithm for deciphering modern detrital processes from lake sediments of Lake Donggi Cona, NE Tibetan Plateau, China. Sedimentary Geology 243, 169–180.

Dietze, M., Kreutzer, S., Burow, C., Fuchs, M.C., Fischer, M., Schmidt, C., 2016. The abanico plot: visualising chronometric data with individual standard errors. Quat. Geochronol. 31, 12–18.

Dietze, E., Maussion, F., Ahlborn, M., Diekmann, B., Hartmann, K., Henkel, K., Kasper, T., Lockot, G., Opitz, S., Haberzettl, T., 2013a. Sediment transport processes across the Tibetan Plateau inferred from robust grain size end-members in lake sediments. Clim. Past 9, 4855–4892.

Dietze, E., Wünnemann, B., Hartmann, K., Diekmann, B., Jin, H., Stauch, G., Yang, S., Lehmkuhl, F., 2013b. Early to mid-Holocene Lake high-stand sediments at Lake Donggi Cona, northeastern Tibetan Plateau, China. Quat. Res. 79, 325–336.

Dixey, F., 1956. The east African rift system. HM Stationery Office.

Doucouré, C.M., de Wit, M.J., 2003. Old inherited origin for the present near-bimodal topography of Africa. J. Afr. Earth Sci. 36 (4), 371–388.

Duller, G.A.T., 2015. The analyst software package for luminescence data: overview and recent improvements. Ancient TL 33, 35–42.

Durcan, J.A., King, G.E., Duller, G.A.T., 2015. DRAC: dose rate and age calculator for trapped charge dating. Quat. Geochronol. 28, 54–61.

Eckardt, F.E., Flügel, T., Cotterill, F., Rowe, C., McFarlane, M., 2016. Kalahari tectonic landforms and processes beyond the Okavango Graben. Quat. Int. 404, 194.

Fairhead, J.D., Girdler, R.W., 1969. How far does the rift system extend through Africa? Nature 221 (5185), 1018–1020.

Folk, R.L., 1954. The distinction between grain size and mineral composition in sedimentary-rock nomenclature. J. Geol. 62, 344–359.

Folk, R.L., Ward, W.C., 1957. Brazos River bar: a study in the significance of grain size parameters. J. Sediment. Petrol. 27 (1), 3–26.

Galbraith, R.F., Roberts, R.G., Laslett, G.M., Yoshida, H., Olley, J.M., 1999. Optical dating of single and multiple grains of quartz from jinmium rock shelter, northern Australia: part I, experimental design and statistical models. Archaeometry 41, 339–364.

Gawthorpe, R.L., Hurst, J.M., 1993. Transfer zones in extensional basins: their structural style and influence on drainage development and stratigraphy. J. Geol. Soc. Lond. 150, 1137–1152.

Google Earth, 2020. Chobe region, Botswana. Pro V 7.3.4.8573, CNES/Airbus 2020. http://www.earth.google.com.

Grove, A.T., 1969. Landforms and climatic change in the Kalahari and Ngamiland. Geogr. J. 135 (2), 191–212.

Guérin, G., Mercier, N., Adamiec, G., 2011. Dose-rate conversion factors: update. Ancient TL 29 (1), 5–8.

Guérin, G., Mercier, N., Nathan, R., Adamiec, G., Lefrais, Y., 2012. On the use of the infinite matrix assumption and associated concepts: a critical review. Radiat. Meas. 47 (9), 778–785.

Gumbricht, T., McCarthy, T.S., Merry, C.L., 2001. The topography of the Okavango Delta, Botswana, and its tectonic and sedimentological implications. S. Afr. J. Geol. 104 (3), 243–264.

Günther, T., Rücker, C., 2019. Boundless Electrical Resistivity Tomography BERT v2. 2–The User Tutorial. LIAG Hannover, TU Berlin, 338 pp. http://www.resistivity.net/download/bert-tutorial.pdf.

Holbrook, J., Schumm, S.A., 1999. Geomorphic and sedimentary response of rivers to tectonic deformation: a brief review and critique of a tool for recognizing subtle epeirogenic deformation in modern and ancient settings. Tectonophysics 305 (1–3), 287–306.

Huntsman-Mapila, P., Kampunzu, A.B., Vink, B., Ringrose, S., 2005. Cryptic indicators of provenance from the geochemistry of the Okavango Delta sedimentsBotswana. Sedimentary Geology 174 (1–2), 123–148.

Huntsman-Mapila, P., Tiercelin, J.J., Benoit, M., Ringrose, S., Diskin, S., Cotten, J., Hémond, C., 2009. Sediment geochemistry and tectonic setting: Application of discrimination diagrams to early stages of intracontinental rift evolution, with examples from the Okavango and Southern Tanganyika rift basins. J. Afr. Earth Sci. 53 (1–2), 33–44.

Keller, E.A., Pinter, N., 1996. Active Tectonics. Prentice-Hall, Upper Saddle River, 338 pp.

Kim, J.C., Duller, G.A.T., Roberts, H.M., Wintle, A.G., Lee, Y.I., Yi, S.B., 2009. Dose dependence of thermally transferred optically stimulated luminescence signals in quartz. Radiat. Meas. 44 (2), 132–143.

Kinabo, B.D., Atekwana, E.A., Hogan, J.P., Modisi, M.P., Wheaton, D.D., Kampunzu, A. B., 2007. Early structural development of the Okavango rift zoneNW Botswana. J. Afr. Earth Sci. 48, 125–136.

Kinabo, B.D., Hogan, J.P., Atekwana, E.A., Abdelsalam, M.G., Modisi, M.P., 2008. Fault growth and propagation during incipient continental rifting: Insights from a combined aeromagnetic and shuttle Radar Topography Mission digital elevation model investigation of the Okavango Rift Zone, Northwest Botswana. Tectonics 27, TC3013Natu.

Kreutzer, S., Schmidt, C., Fuchs, M.C., Dietze, M., Fischer, M., Fuchs, M., 2012. Introducing an R package for luminescence dating analysis. Ancient TL 30 (1), 1–8.

Loke, M.H., 2004. Rapid 2-D Resistivity & IP inversion using the least-squares method. Wenner (a,b,g), dipole-dipole, inline pole-pole, pole-dipole, equatorial dipole-dipole, Wenner-Schlumberger and non-conventional arrays on land, underwater and cross-borehole surveys. In: RES2DINV ver. 3.54 Manual. Geotomo Software.

Loke, M.H., Barker, R.D., 1996. Rapid least-squares inversion of apparent resistivity pseudosections by a quasi-Newton method1. Geophys. Prospect. 44 (1), 131–152.

Mallick, D.I.J., Habgood, F., Skinner, A.C., 1981. A geological interpretation of Landsat imagery and air photography of Botswana. In: Overseas Geology and Mineral Resources, 56. Institute of Geological Sciences, London, 36 pp.

Mauz, B., Lang, A., 2004. Removal of the feldspar-derived luminescence component from polymineral fine silt samples for optical dating applications: evaluation of chemical treatment protocols and quality control procedures. Ancient TL 22 (1), 1–8.

McCarthy, T.S., 2013. The Okavango Delta and its place in the geomorphological evolution of southern Africa. S. Afr. J. Geol. 116 (1), 1–54.

McFarlane, M.J., Eckardt, F.D., 2007. Palaeodune morphology associated with the Gumare fault of the Okavango graben in the Botswana/Namibia borderland: a new model of tectonic influence. S. Afr. J. Geol. 110 (4), 535–542.

Modisi, M.P., Atekwana, E.A., Kampunzu, A.B., Ngwisanyi, T.H., 2000. Rift kinematics during the incipient stages of continental extension: evidence from the nascent Okavango rift basin, Northwest Botswana. Geology 28 (10), 939–942.

Mokatse, T., Diaz, N., Shemang, E., Van Thuyne, J., Vittoz, P., Vennemann, T., Verrecchia, E.P., 2022. Landscapes and landforms of the Chobe Enclave, Northern Botswana. In: Eckardt, F. (Ed.), Landscapes and Landforms of Botswana. Springer-Nature, Dordrecht, pp. 91–116. https://doi.org/10.1007/978-3-030-86102-5_6.

Moore, A.E., 1999. A reappraisal of epeirogenic flexure axes in southern Africa. S. Afr. J. Geol. 102, 363–376.

Moore, A.E., Cotterill, F.P.D., Eckardt, F.D., 2012. The evolution and ages of Makgadikgadi palaeo-lakes: consilient evidence from Kalahari drainage evolution south-central Africa. S. Afr. J. Geol. 115 (3), 385–413.

Moorkamp, M., Fishwick, S., Walker, R.J., Jones, A.G., 2019. Geophysical evidence for crustal and mantle weak zones controlling intra-plate seismicity–the 2017 Botswana earthquake sequence. Earth Planet. Sci. Lett. 506, 175–183.

Murray, A.S., Wintle, A.G., 2000. Luminescence dating of quartz using an improved single-aliquot regenerative-dose protocol. Radiat. Meas. 32, 57–73.

NASA JPL, 2013. NASA shuttle radar topography mission global 1 arc second. In: Nasa Lp Daac, p. 15.

Nash, D.J., Eckardt, F.D., 2015. Drainage development, neotectonics and base-level change in the Kalahari Desert, southern Africa. S. Afr. Geogr. J. 98 (2), 308–320.

Neal, A., 2004. Ground-penetrating radar and its use in sedimentology: principles, problems and progress. Earth Sci. Rev. 66 (3–4), 261–330.

Otvos, E.G., 2000. Beach ridges—definitions and significance. Geomorphology 32 (1–2), 83–108.

Parsons, A.J., Abrahams, A.D., 2009. Geomorphology of desert environments. In: Parsons, A.J., Abrahams, A.D. (Eds.), Geomorphology of Desert Environments. Springer Nature, Dordrecht, pp. 3–7.

Partridge, T.C., 1998. Of diamonds, dinosaurs and diastrophism: 150 million years of landscape evolution in southern Africa. S. Afr. J. Geol. 101 (3), 167–184.

Pastier, A.-M., Dauteuil, O., Murray-Hudson, M., Moreau, F., Walpersdorf, A., Makati, K., 2017. Is the Okavango Delta the terminus of the East African Rift System? Towards a new geodynamic model: geodetic study and geophysical review. Tectonophysics 712–713, 469–481.

Podgorski, J.E., Green, A.G., Kgotlhang, L., Kinzelbach, W.K., Kalscheuer, T., Auken, E., Ngwisanyi, T., 2013. Paleo-megalake and paleo-megafan in southern Africa. Geology 41 (11), 1155–1158.

Prins, M.A., Bouwer, L.M., Beets, C.J., Troelstra, S.R., Weltje, G.J., Kruk, R.W., Vroon, P. Z., 2002. Ocean circulation and iceberg discharge in the glacial North Atlantic: Inferences from unmixing of sediment size distributions. Geology 30 (6), 555–558.

Prins, M.A., Vriend, M., Nugteren, G., Vandenberghe, J., Lu, H., Zheng, H., Weltje, G.J., 2007. Late Quaternary aeolian dust input variability on the Chinese Loess Plateau: inferences from unmixing of loess grain-size records. Quat. Sci. Rev. 26 (1–2), 230–242.

R Core Team, 2021. R: A Language and Environment for Statistical Computing. R Foundation for Statistical Computing, Vienna, Austria. https://www.R-project.org/.

Rhea, S., 1993. Geomorphic observations of rivers in the Oregon Coast Range from a regional reconnaissance perspective. Geomorphology 6 (2), 135–150.

Ringrose, S., Downey, B., Genecke, D., Sefe, F., Vink, B., 1999. Nature of sedimentary deposits in the western Makgadikgadi basinBotswana. J. Arid Environ. 43 (4), 375–397.

Ringrose, S., Huntsman-Mapila, P., Kampunzu, H., Downey, W.D., Coetzee, S., Vink, B., Vanderpost, C., 2005. Geomorphological and geochemical evidence for palaeo feature formation in the northern Makgadikgadi sub-basin, Botswana. Palaeogeogr. Palaeoclimatol. Palaeoecol. 217, 265–287.

Ringrose, S., Harris, C., Huntsman-Mapila, P., Vink, B.W., Diskins, S., Vanderpost, C., Matheson, W., 2009. Origins of strandline duricrusts around the Makgadikgadi Pans (Botswana Kalahari) as deduced from their chemical and isotope composition. Sediment. Geol. 219 (1–4), 262–279.

Riquelme, R., Martinod, J., Hérail, G., Darrozes, J., Charrier, R., 2003. A geomorphological approach to determining the Neogene to recent tectonic deformation in the Coastal Cordillera of northern Chile (Atacama). Tectonophysics 361 (3–4), 255–275.

Ruszkiczay-Rüdiger, Z., Fodor, L., Horváth, E., Telbisz, T., 2009. Discrimination of fluvial, eolian and neotectonic features in a low hilly landscape: a DEM-based morphotectonic analysis in the Central Pannonian BasinHungary. Geomorphology 104 (3–4), 203–217.

Schmidt, C., Zeeden, C., Krauß, L., Lehmkuhl, F., Zöller, L., 2021. A chronological and palaeoenvironmental re-evaluation of two loess-palaeosol records in the northern Harz foreland, Germany, based on innovative modelling tools. Boreas 50, 746–763.

Schumm, S.A., Dumont, J.F., Holbrook, M.J., 2002. Active Tectonics and Alluvial Rivers. In: Cambridge University Press, Cambridge, p. 276.

Silva, P.G., Goy, J.L., Zazo, C., Bardaj, T., 2003. Fault-generated mountain fronts in Southeast Spain: geomorphologic assessment of tectonic and seismic activity. Geomorphology 50 (1–3), 203–225.

Shaw, P.A., Cooke, H.J., 1986. Geomorphic evidence for the late Quaternary palaeoclimates of the middle Kalahari of northern Botswana. Catena 13 (4), 349–359.

Shaw, P.A., Thomas, D.S.G., 1988. Lake Caprivi: a late Quaternary link between the Zambezi and middle Kalahari drainage systems. Z. Geomorphol. 32 (3), 329–337.

Shaw, P.A., Cooke, H.J., Thomas, D.S.G., 1988. Recent advances in the study of Quaternary landforms in Botswana. In: Collection Palaeoecology of Africa, 19, pp. 15–26.

Shaw, P.A., Stokes, S., Thomas, D.S.G., Davies, F.B.M., Holmgren, K., 1997. Palaeoecology and age of a Quaternary high lake level in the Makgadikgadi Basin of the Middle KalahariBotswana. South African Journal of Science 93 (6), 273–276.

Stolt, R.H., 1978. Migration by Fourier transform. Geophysics 43, 23–48.

Storz, H., Storz, W., Jacobs, F., 2000. Electrical resistivity tomography to investigate geological structures of the earth's upper crust. Geophys. Prospect. 48 (3), 455–472.

Vainer, S., Erel, Y., Matmon, A., 2018. Provenance and depositional environments of Quaternary sediments in the southern Kalahari Basin. Chem. Geol. 476, 352–369.

Vainer, S., Matmon, A., Erel, Y., Hidy, A.J., Crouvi, O., De Wit, M., Geller, Y., Team, A.S. T.E.R., 2021. Landscape responses to intraplate deformation in the Kalahari constrained by sediment provenance and chronology in the Okavango Basin. Basin Research 33 (2), 1170–1193.

Vainer, S., Matmon, A., Dor, Y.B., Verrecchia, E., Eckardt, F.D, Team, A.S.T.E.R, 2021. Eolian chronology reveals causal links between tectonics, climate, and erg generation. In: Royal, S. (Ed.), PRE_PRINT-Researchsquare. https://doi.org/10.21203/rs.3.rs-801542/v1.

Van Thuyne, J., Darini, I., Mainga, A., Verrecchia, E.P., 2021. Are fungus-growing termites super sediment-sorting insects of subtropical environments? J. Arid Environ. 193, 104566.

Wisen, R., Auken, E., Dahlin, T., 2005. Combination of 1D laterally constrained inversion and 2D smooth inversion of resistivity data with a priori data from boreholes. In: Near Surface Geophysics, 3. European Association of Geoscientists & Engineers, pp. 71–79.

Yu, Y., Gao, S.S., Moidaki, M., Reed, C.A., Liu, K.H., 2015a. Seismic anisotropy beneath the incipient Okavango rift: implications for rifting initiation. Earth Planet. Sci. Lett. 430, 1–8.

Yu, Y., Liu, K.H., Moidaki, M., Reed, C.A., Gao, S.S., 2015b. No thermal anomalies in the mantle transition zone beneath an incipient continental rift: evidence from the first receiver function study across the Okavango rift zoneBotswana. Geophys. J. Int. 202 (2), 1407–1418.

Yu, Y., Liu, K.H., Huang, Z., Zhao, D., Reed, C.A., Moidaki, M., Lei, J., Gao, S.S., 2017. Mantle structure beneath the incipient Okavango rift zone in southern Africa. Geosphere 13 (1), 102–111.